Comparing Functional MRI Protocols for Small, Iron-Rich Basal Ganglia Nuclei Such as the Subthalamic Nucleus at 7 T and 3 T

Gilles de Hollander,[1,2] **Max C. Keuken**,[1,2] **Wietske van der Zwaag**,[3] **Birte U. Forstmann**,[1,2,4]* **and Robert Trampel**[5]

[1]*University of Amsterdam, Amsterdam Brain & Cognition Center, Amsterdam, The Netherlands*
[2]*Netherlands Institute for Neuroscience, an Institute of the Royal Netherlands Academy of Arts and Sciences, Amsterdam, The Netherlands*
[3]*Spinoza Centre for Neuroimaging, Amsterdam, The Netherlands*
[4]*Department of Psychology, Universiteit Leiden, Leiden, The Netherlands*
[5]*Max Planck Institute for Human Cognitive and Brain Sciences, Leipzig, Germany*

Abstract: The basal ganglia (BG) form a network of subcortical nuclei. Functional magnetic resonance imaging (fMRI) in the BG could provide insight in its functioning and the underlying mechanisms of Deep Brain Stimulation (DBS). However, fMRI of the BG with high specificity is challenging, because the nuclei are small and variable in their anatomical location. High resolution fMRI at field strengths of 7 Tesla (T) could help resolve these challenges to some extent. A set of MR protocols was developed for functional imaging of the BG nuclei at 3 T and 7 T. The protocols were validated using a stop-signal reaction task (Logan et al. [1984]: J Exp Psychol: Human Percept Perform 10:276–291). Compared with submillimeter 7 T fMRI protocols aimed at cortex, a reduction of echo time and spatial resolution was strictly necessary to obtain robust Blood Oxygen Level Dependent (BOLD) sensitivity in the BG. An fMRI protocol at 3 T with identical resolution to the 7 T showed no robust BOLD sensitivity in any of the BG nuclei. The results suggest that the subthalamic nucleus, as well as the substantia nigra, red nucleus, and the internal and external parts of the globus pallidus show increased activation in failed stop trials compared with successful stop and go trials. *Hum Brain Mapp 00:000–000, 2017.*

Key words: ultra-high field MRI; functional neuroimaging; basal ganglia; subthalamic nucleus; stop-signal reaction task

INTRODUCTION

The basal ganglia (BG) are a set of subcortical nuclei (the subthalamic nucleus, STN; the substantia nigra, SN; the globus pallidus, pars interna, GPi; the globus pallidus, pars externa, GPe; and the striatum, STR), that play a crucial role in functions such as action selection, cognitive control, and response inhibition [Alexander and Crutcher, 1990; Aron, 2011; Frank, 2006; Middleton and Strick, 2000; Parent and Hazrati, 1995; Redgrave et al., 1999; Redgrave et al., 2010]. These nuclei project to large parts of the cortex, possibly within discrete "cortical-subcortical loops" that correspond to different functional domains such as

Additional Supporting Information may be found in the online version of this article.

The authors declare no competing financial interest.

Contract grant sponsors: Starter Grant from the European Research Council (ERC; BUF) and a Vidi grant from the Netherlands Organization for Scientific Research (NWO; BUF).

*Correspondence to: B. U. Forstmann; Nieuwe Achtergracht 130, 1018 VZ Amsterdam, The Netherlands. E-mail: buforstmann@gmail.com

Received for publication 23 November 2016; Revised 9 March 2017; Accepted 15 March 2017.

DOI: 10.1002/hbm.23586

Published online 00 Month 2017 in Wiley Online Library (wileyonlinelibrary.com).

cognition, motor control, and emotion [Alexander and Crutcher, 1990; Keuken et al., 2012; Temel et al., 2005]. Malfunctioning of the BG is implicated in many clinical conditions, including Parkinson's disease (PD), Huntington's chorea, schizophrenia, attention deficit disorder (ADHD), and addiction.

Deep brain stimulation (DBS) of BG nuclei, in particular the STN, is an important therapy in PD. However, the precise underlying mechanisms of this therapy are poorly understood and severe side-effects can occur, possibly because of modulations of different cortical–subcortical loops than the motor control loop [Fasano and Lozano, 2015; Ineichen et al., 2014; Temel et al., 2005].

Functional neuroimaging in healthy and clinical human populations could help elucidate the functional mechanisms of the BG in health and disease, as well as provide a mechanistic explanation of therapeutic benefits and side-effects of DBS. However, in the BG the anatomical specificity of traditional functional Magnetic Resonance Imaging (fMRI) techniques is limited, because the nuclei in the BG are very small compared with the voxel size of most functional MRI protocols. For example, with a voxel size of 3 mm isotropic, a commonly used voxel size in 3 T fMRI studies, the entire STN can be covered in 4–5 voxels, assuming only small partial volume effects [the STN has a volume of approximately 100 mm^3; de Hollander et al., 2015; Keuken et al., 2014; Zwirner et al., 2017]. This is especially problematic because a related nucleus, the SN, lies directly adjacent to the STN (and also other related nuclei, such as the red nucleus, RN, are only a few millimeters away). At lower resolutions, it becomes very likely, due to partial volume effects, that functional signals from the SN are intermixed with those from the STN [de Hollander et al., 2015]. A related problem is that individual anatomy is usually not taken into account: it is assumed that whole-brain registration to a standard space (e.g., MNI152), based mostly on image contrast between gray and white matter in cortex, is sufficient to achieve millimeter precision and perfect across-subject anatomical overlap of subcortical nuclei in the standard space. This assumption is problematic. An anatomically more precise approach would entail labeling the nuclei-of-interest in individual space. However, visualizing the location of the nuclei of the BG in the individual brain at lower field strengths than 7 T is very challenging [De Hollander et al., 2015; Plantinga et al., 2014; Schäfer et al., 2011].

The use of Ultra-High Field Magnetic Resonance Imaging (UHF-MRI; MRI with field strengths of 7 T and above) could help increase the anatomical specificity of functional neuroimaging of the BG, because its increased signal-to-noise ratios (SNR) potentially allow for substantially decreased voxel sizes of less than one millimeter isotropic [Van der Zwaag et al., 2016]. The increased spatial specificity, combined with the high-quality structural images at UHF-MRI, permits the testing of hypotheses about the functional specialization of the different BG nuclei, as well as putative subdivisions within these nuclei. For example, a prominent theory about the STN is that it has three subdivisions, distinctly connected to "motor," "cognitive," and "limbic" cortical networks [Keuken et al., 2012; Temel et al., 2005].

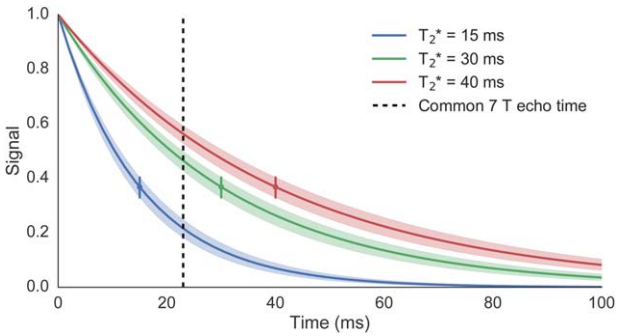

Figure 1.

Signal decay curves for different T_2* relaxation value. At 7 T, the T_2* relaxation value for STN is approximately 15 ms, whereas the relaxation time in the cortex is approximately 30–40 ms. The dotted line indicates a common echo time at 7 T of 22 ms. Clearly, the signal in the cortex is still strong at this point in time, but the signal in the STN has largely faded. Colored dots indicate the signal of the T_2* curve at its respective T_2* value. The shaded area shows the change in signal corresponding to a T_2* value up- or downshift of 10%. Note that the size of this signal change is largest around the baseline T_2* value. [Color figure can be viewed at wileyonlinelibrary.com]

However, experiences in and outside of our lab suggest that "off-the-shelf" fMRI protocols at 7 T, originally developed for functional imaging in the cortex, do not achieve an acceptable temporal signal-to-noise ratio (tSNR) in the BG, precluding robust Blood Oxygen Level Dependent (BOLD) sensitivity [see also Barry et al., 2013].

The low tSNR obtained in the BG with UHF fMRI is most likely due to a combination of at least three complicating factors. First, the BG have very high concentrations of iron, which leads to substantially reduced T_2* relaxation values, especially at higher field strengths [Aquino et al., 2009; De Hollander et al., 2014; Deistung et al., 2013; Keuken et al., 2013; Langkammer et al., 2012; Schweser et al., 2011]. The phenomenon underlying all common fMRI measurements is the so-called BOLD-effect [Ogawa et al., 1990]: a difference in T_2* relaxation values between paramagnetic deoxyhemoglobin and diamagnetic oxyhemoglobin, as well as the dynamics in the vasculature surrounding neural tissue [Logothetis, 2008]. The theoretically optimal echo time (TE) for a single-echo T_2* weighted fMRI protocol is therefore equal to the baseline T_2* of the tissue-of-interest [Norris, 2006]. At this point during the decay, the shift in signal resulting from a small change in T_2* is greatest (see Fig. 1). One of the main advantages of UHF-MRI is the increased contrast in T_2* weighted images, because there is more variance in T_2* relaxation values

TABLE I. Parameters of the fMRI protocols that were tested

MR parameter	Protocol 1	Protocol 2	Protocol 3	Protocol 4
Field strength	7 T	7 T	7 T	3 T
Resolution	$1.2 \times 1.2 \times 1.2$ mm^3	$1.2 \times 1.2 \times 1.2$ mm^3	$1.5 \times 1.5 \times 1.5$ mm^3	$1.5 \times 1.5 \times 1.5$ mm^3
TE	22 ms	15 ms	14 ms	30 ms
TR	2 s	2 s	2 s	2 s
Flip angle	75°	75°	60°	81°
Grappa factor	4	4	3	2
Matrix size	150×150	150×150	128×128	64×64
Bandwidth	1,450 Hz/Px	1,450 Hz/Px	1,446 Hz/Px	1,396 Hz/Px
Partial Fourier	6/8	6/8	6/8	–
Total number of subjects	5	5	20	10

across the brain [Peters et al., 2007; Van der Zwaag et al., 2016]. However, this increase in variability of baseline T_2* relaxation times across the brain also comes with increased variability in the optimal TE for fMRI. The baseline T_2* relaxation value for the cortex is approximately 25–35 ms at 7 T, whereas the baseline T_2* relaxation value for the STN in young healthy participants, as well as most other BG nuclei in the subcortex, is roughly 15 ms [Keuken et al., 2013; Peters et al., 2007; Van der Zwaag et al., 2009; Yacoub et al., 2001]. Hence, the TE of most echo-planar based (EPI) protocols at 7 T targeted at cortex is too long to acquire a reliable BOLD contrast in the BG: the MR signal has almost completely decayed by the time of signal readout.

A second complicating factor for UHF fMRI in the BG is its location deep in the brain. As a consequence, the BG lie relatively far from the receive elements of a typical head coil, as well as approximately equidistant to them. The sensitivity of the different receiver coils to signal from the BG is therefore not only relatively low, but also roughly equal across coils. Therefore, parallel imaging techniques, such as GRAPPA and SENSE are less effective in the BG, because they exploit differences in the sensitivity profiles of the receiver coils. This well-known issue of having a higher noise level in the center of the brain when using parallel imaging techniques is called "g-factor penalty" [De Zwart et al., 2002; Griswold et al., 2002; Pruessmann et al., 1999; Setsompop et al., 2016; Sodickson and Manning, 1997]. In whole-brain UHF fMRI this is especially unfortunate, because at such high field strengths, parallel imaging is essential. The increased resolution in UHF fMRI, resulting in prolonged echo trains, as well as reduced T_2* relaxation values, call for parallel imaging to overcome geometric distortions, and to achieve sufficiently short TE's and acceptable temporal resolution [De Zwart et al., 2002; Setsompop et al., 2016; Van der Zwaag et al., 2016].

A third complicating factor is the relatively increased physiological noise at UHF compared with lower field strengths [Triantafyllou et al., 2005]. It is well known that cardiac and respiratory artifacts are especially prominent in the more inferior parts of the brain, close to areas of major cerebral spinal fluid (CSF) flow, such as the interpeduncular fossa, and junctions of major arteries such as the circle of Willis. However, Barry et al. [2013] showed that although signal variance is much higher in the subcortex than in cortex, only little of this variance can be explained by cardiac, respiratory, and CSF dynamics in 7 T fMRI. The authors speculated that these unexplained sources of noise might have a neural origin and are related to intrinsic functional connectivity, unrelated to the particular task at hand [Barry et al., 2013]. These results suggest that the task-related BOLD contrast in subcortex is contaminated with noise that is difficult to filter out using physiological regressors.

Therefore, in order to detect neural activity in the STN, in this study we investigated the BOLD sensitivity of multiple fMRI protocols with different parameter sets using 7 T MRI in the BG. We asked how TE and resolution can be adjusted such that the aforementioned problems can be overcome and an optimal combination of BOLD sensitivity and spatial and temporal resolution is achieved (see Table I). In addition to TE and resolution, acceleration factors were also systematically covaried with resolution. Higher resolutions lead to longer readout times. Therefore, the acceleration factors of the protocols at the highest resolution also had to be increased, to obtain sufficiently short TEs. The protocols were evaluated while participants performed a stop-signal task, a prominent paradigm in cognitive neuroscience and for which ample work suggests that especially the STN plays an important role [Aron, 2006, 2007; Aron et al., 2014b]. Drawing on other prominent neurocomputational models of the role of the BG in perceptual decision-making and action control, we speculated that other BG nuclei would likely also show heightened activity in all conditions when compared with baseline [Bogacz and Gurney, 2007; Frank and Claus, 2006; Gurney et al., 2001].

Recently, BOLD activity was reported in small subcortical nuclei in the subcortex at lower field strengths [3 T and below; de Hollander et al., 2015], and even functional subdivisions in the substantia nigra were reported in a study using 3T [Pauli et al., 2015]. As functional magnetic resonance imaging at 3 T is much less costly and challenging than at higher fields, ultra-high field fMRI should only

be used when lower-field strengths cannot provide the necessary BOLD sensitivity and anatomical specificity. Therefore, to justify the need for 7 T fMRI, we also directly compared BOLD sensitivity of a 3 T protocol to the best-performing 7 T protocol, using the same resolution and an identical experimental paradigm, but otherwise parameters optimized for 3 T. The 3 T protocol was as similar as possible to the protocol reported in the recent study by Pauli et al. [2015] that reported functional subdivisions in the SN.

METHODS

Structural MRI

Identifying the nuclei of the BG in individual anatomical scans is crucial to distinguish BOLD signals from different nuclei, but remains a challenge, especially at 3 T [de Hollander et al., 2015]. Therefore, for 14 participants, high-quality anatomical scans acquired at 7 T and individual anatomical BG masks of an earlier study by Keuken et al. [2014] were used. The masks were based on a set of multi-echo T_2* weighted anatomical FLASH volumes at a resolution of 0.5 mm isotropic [Forstmann et al., 2014; Haase et al., 1985]. These T_2* weighted images were used to draw masks of the SN, STN, and RN following a strict protocol (see Keuken et al., 2014 for details). They were also used to calculate Quantitative Susceptibility Mapping images [QSM; Langkammer et al., 2012]. These QSM images were used to draw individual anatomical masks of the GPi and GPe. The masks were drawn by two independent, trained raters. The conjunct voxels of these two masks were used as the final Region-of-Interest (ROI) in all analyses. In other words, only voxels that were labeled as inside the nucleus-of-interest by both raters were used for signal extraction. Exploratory analyses using disjunctive masks (containing all voxels rated as in-the-nucleus by at least one of the raters) showed comparable results as those with the conjunct masks, indicating that the choice for conjunct masks is not crucial for our results.

For the remaining six participants, an identical anatomical 7 T scan and anatomical labeling protocol as in the original Keuken et al. (2014) study was performed specifically for this study.

For all participants, a 0.7 mm isotropic T_1 weighted image was acquired using the MP2RAGE sequence at 7 T [Marques et al., 2010] with the following parameters: repetition time (TR) = 5,000 ms; TE = 2.45 ms; inversion times TI1 = 900; TI2 = 2,750 ms; flip angle 1 = 5°; flip angle 2 = 3°. This anatomical scan was used to allow for registration and transformation of statistical parametric maps (SPMs) to MNI152 standard space.

Also at the 3 T scanner, anatomical images were collected. The anatomical image used here was based on a 4-echo 1 mm isotropic FLASH protocol (128 slices; TEs of 9.84 ms, 17.22 ms, 24.60 ms, and 31.98 ms; TR = 43 ms, flip angle = 15°). The resulting T_2* weighted images were used to estimate T_2* relaxation times for the different nuclei-of-interest at 3 T. Also, these data were registered to the 7 T FLASH images and the 3 T functional data. The resulting transformation matrices were used to transform the individual anatomical masks based on the 7 T FLASH images to the 3 T functional data.

Functional MRI Protocols

Three different 2D-EPI protocols were tested at 7 T (see Table I). Protocol 1 and 2 were designed to have a relatively high spatial resolution (1.2 mm isotropic) and were equal in all parameters, except TE (22 vs. 15 ms). Protocol 1 and 2 were thus designed to investigate the effect of TE on the detected BOLD signal. For protocol 3, to increase SNR at the cost of spatial specificity, the voxel resolution was considerably reduced to 1.5 mm isotropic. This led to smaller matrix sizes and readout times, so the GRAPPA factor and echo time could be decreased, yielding a higher SNR. We chose to optimize parameters as much as possible for a given resolution, rather than doing an exhaustive, full parameter sweep, which would be extremely expensive. In other words: we chose not to run protocol 3 with a GRAPPA-factor of 4, like protocol 1 and 2, because it was not necessary at that resolution and would be detrimental to the image quality.

Protocols 1–3 were acquired at a Siemens MAGNETOM 7 T system (Siemen Medial Solutions, Erlangen, Germany), using a 32-channel head array Nova coil (NOVA Medical Inc., Wilmington MA). For protocol 1, which consisted of 3 runs of 515 volumes with 38 slices, respectively, the acquisition time was 17:10 min per run. The other parameters were as follows: TR = 2,000 ms, TE = 22 ms, flip angle = 75°, bandwidth 1450 Hz/Px, echo spacing 0.81 ms, voxel size = 1.2 mm isotropic, Field-of-View (FOV) 180 × 180 × 45.6 mm, phase encoding direction A ≫ P, partial Fourier 6/8, GRAPPA acceleration factor 4, matrix size 150 × 150.

Protocol 2 was identical, except that the TE was decreased to 15 ms.

Note that the Ernst angle for the STN is approximately 80°, assuming a T1 value of approximately 1,200 ms [Keuken et al., 2017]. However, because of limitations due to the Specific Absorption Rate (SAR), for protocol 1 and 2, a flip angle of 75° was used.

Protocol 3 also consisted of 3 runs of 515 volumes and it also took 17:10 min to acquire. This protocol entailed 60 slices with a voxel size of 1.5 mm isotropic. This allowed for a FOV that covered almost the entire brain, but excluded the most superior part of the brain for most participants. The other parameters were as follows: TR = 2,000 ms, TE = 14 ms, flip angle = 60°, bandwidth 1446 Hz/Px, echo spacing 0.8 ms, FOV 192 × 192 × 97mm, phase encoding direction A ≫ P, partial Fourier 6/8, GRAPPA acceleration factor 3, matrix size 128 × 128. Again, because of SAR restrictions, it was not possible to use the Ernst angle for imaging the STN. Instead, because of the higher

number of slices compared with protocols 1 and 2, for protocol 3, the flip angle had to be further decreased to 60°. Due to its larger FOV, protocol 3 contained large parts of the cortex. These cortical areas are more affected by geometrical distortions due to field inhomogeneities than is the subcortex. Therefore, when acquiring protocol 3, a corresponding B0 field map with the same FOV was acquired (TR = 1,500 ms, TE_1 = 6 ms, TE_2 = 7.02 ms).

Protocol 4 was set up to be able to assess the BOLD sensitivity at 3 T, for a similar resolution as the 7 T protocol. It was an adaptation of the protocol reported by Pauli et al. [2015] and was acquired at a Siemens MAGNETOM Verio 3 Tesla system with a 24-channel head coil. This protocol also consisted of three runs of 515 volumes, but only 26 slices, and at a resolution of 1.5 mm isotropic. The other parameters were: TR of 2,000 ms, TE = 30 ms, flip angle = 81°, bandwidth 1,396 Hz/Px, echo spacing 0.95 ms, FOV 96 × 96 × 39mm with 50% oversampling in the phase-direction, phase encoding direction A ≫ P, no partial Fourier, GRAPPA acceleration factor 2, matrix size 64 × 64.

All four protocols were planned in such a way that all nuclei-of-interest (STN, SN, GPe, GPi, and RN) fell well within the FOV. This was achieved by a slightly tilted axial slice orientation. For protocol 3 we ensured that the inferior frontal gyrus also fell within the FOV. The inferior frontal gyrus has been implicated in response inhibition in many previous studies and used as a 'control region' for the BOLD sensitivity in cortical regions [Aron et al., 2014b, 2015; Erika-Florence et al., 2014].

Physiological data

For estimating the effects of physiological noise on the fMRI data, we recorded physiological data for 6 of the participants in protocol 3. For these 6 participants, the fit of a 32-regressors RETROICOR model [Glover et al., 2000] showed high explained variance in inferior regions around the brainstem and circle of Willis, indicating that the physiological noise modeling was successful. However, analyses showed that the effects of physiological filtering on BOLD sensitivity were very limited [in accordance with Barry et al., 2011; Van der Zwaag et al., 2015]. In the 6 participants for which physiological data was collected, ROI-wise tSNR increased only very marginally after physiological filtering: from 89.2 (std. 22.2) to 95.8 (25.1) in left STN and from 90.3 (sd 21.5) to 96.9 (24.0) in right STN. This is a very limited increase, considering that 32 physiological regressors were filtered out. Accordingly, the statistics of the ROI-based contrast between go trials and failed stop trials were not meaningfully affected. The *t*-statistic of the contrast slightly increased after filtering in left STN ($t(5) = 1.97$, $P = 0.10$ before, $t(5) = 2.3$, $P = 0.07$), whereas it slightly decreased in right STN ($t(5) = 2.93$, $P = 0.03$ before filtering, $t(5) = 2.62$, $P = 0.05$ after filtering). The other nuclei showed similar results. We therefore decided to analyze all data in the same way, without the application of any physiological noise filtering.

TABLE II. Subgroups of participants that were scanned using the different protocols

Group	*n*	Protocol 1	Protocol 2	Protocol 3	Protocol 4
Group A	4	x	x	x	x
Group B	1	x	x	x	
Group C	6			x	x
Group D	9			x	

Participants

In total 20 participants [10 female; mean age 26 (SD 2.6), age range 22–32] took part in the experiment. Participants had normal or corrected-to-normal vision, and none of them had a history of neurological, major medical, or psychiatric disorders as indicated by self-report and structured clinical interview. All participants were right handed, as confirmed by the Edinburgh Inventory (Oldfield, 1971).

The participants that were scanned using the different protocols were largely overlapping. All 20 participants were scanned using protocol 3. Of these 20 participants, 5 participants were also scanned using protocol 1 and 2. Out of these 5 participants, 4 participants were also scanned using protocol 4 (and thereby were scanned using all 4 protocols). Finally, a group of 6 participants (out of the pool of the aforementioned 20 participants) were scanned using protocol 3 and 4 (see also Table II).

The study was approved by the local ethical committee of the University of Leipzig, Germany. All participants gave written informed consent and received a monetary reward for their participation.

Experimental Paradigm

The experimental paradigm consisted of a classic auditory stop-signal task [Aron, 2006; Logan et al., 1984], where participants are instructed to indicate the direction of an arrow using two spatially compatible buttons, as fast as they can. On a subset of trials (25%), participants hear, at some time after stimulus onset (the stop signal delay; SSD), an auditory cue that indicates that they should inhibit their response and not press any button. Longer SSDs usually lead to more failures to stop, because less time remains to inhibit an ongoing response. Following the study of Aron [2006], the SSD is dynamically adapted during scanning, in steps of 50 ms, using a staircase procedure to make sure that each participant successfully stops on approximately 50% of the trials [see also Logan and Cowan, 1984].

Participants performed 384 trials per session (three blocks of 128 trials), including 96 stop trials (32 per block). During protocol 3, one participant performed only 256 out of the 384 trials and another participant performed only 345 out of the 384 trials. Both participants quit because of fatigue (note that the total task time of 3 runs was 51

minutes). We chose to still include these 2 participants in the final analysis of protocol 3, because (a) these participants performed the large majority of the trials, (b) their data could improve the statistical power of this study, (c) the larger variability in their estimates could be modeled in the level 2-analyses.

Each trial lasted 8 seconds (4 fMRI volumes) in total. A trial started with the presentation of a white circle. After 500, 1,000, 1,500, or 2,000 ms, an arrow pointing to the left or right was presented in the middle of the circle, indicating the desired response. The stimulus always disappeared after 1,000 ms regardless of a stop signal or (an inhibited) response. For the remaining 5,000–6,500 ms, a blank screen was presented. The relatively long inter-trial interval was chosen to allow for deconvolving the BOLD signal related to each trial in a model-free manner using finite impulse response functions [FIR; Poldrack et al., 2011].

Behavioral analysis

Standard analyses of behavior during the stop-signal task were performed. The stop-signal task has three conditions of interest: trials in which no stop signal was delivered and the subject gave the correct response (*go* trials), trials in which a stop signal was delivered and the participant gave no response (*successful stop* trials), and trials in which a stop signal was delivered and the participant gave the correct response (*failed stop* trials). There was a small proportion (0.90%) of trials were the participant gave an incorrect response. These trials were excluded from the analysis. Responses that were faster than 150 ms or slower than the stimulus duration of 1,000 ms were also excluded (1.5%). For every participant and experimental session, we calculated the median response time (RT) for go trials, the median RT for failed stop trials and the proportion of successful stops, both per SSD and over all trials.

Lastly, we also calculated the stop signal reaction time (SSRT): an estimate of the average amount of time it takes a participant to inhibit their response after the stop signal has been presented, assuming an independent race between a go and stop process. By mathematically formalizing the cognitive process underlying the stop signal task as a race, we can estimate this SSRT. Specifically, the SSRT was estimated using the so-called "mean method." This method takes the percentile of the Go RT distribution corresponding to the rate of unsuccessful stops (close to 50% for all subjects), and subtracts the mean SSD from this value [Aron, 2006; Logan et al., 1984; Verbruggen and Logan, 2009].

Image registration

For all protocols at 7 T, the mean functional signal intensity images were registered to the middle echo (20.39 ms) of the 0.5 mm isotropic T_2* weighted FLASH images using linear affine transformations, optimized by the ANTS registration algorithm and the mutual information cost function [version 2.0.0; Avants et al., 2009]. Visual inspection revealed that the automatic registration was sufficient.

Multiple registration algorithms and cost functions in FSL FLIRT [Jenkinson and Smith, 2001], MIPAV [Bazin et al., 2007], and ANTS [Avants et al., 2009] were applied to register the 3 T functional data (protocol 4) to the 3 T and 7 T FLASH images. However, after visually inspecting the results, we concluded that it was not feasible to register the 3 T data automatically, because of a lack of contrast-to-noise and the small FOV of the 3 T functional 2D-EPI images. We therefore opted for a manual landmark-based approach. Concretely, one rater (MCK) indicated in both the anatomical 3 T FLASH images and the mean functional 1.5 mm isotropic 3 T 2D-EPI images the location of the following landmarks: the top indentation of the pons, the posterior part of the fourth ventricle, the ventral point of the bilateral RN, and the most anterior–dorsal–lateral part of the bilateral GPe. Then MIPAV [Bazin et al., 2007; McAuliffe et al., 2001] was used to find the linear transformation that minimizes the distance between these manually indicated landmarks in both image modalities. This linear transformation was used in all further processing. The average 3 T FLASH images were also registered to the average 7 T FLASH images using linear registration in FSL FLIRT, to allow for using the anatomical masks drawn on the latter modality for the 3 T data.

The linear transformation matrices from the functional scans to the anatomical T_2* weighted FLASH images were inverted and all the individual anatomical masks (left and right STN, SN, RN, GPi, and GPe) were transformed into individual functional space using nearest-neighbor interpolation. When anatomical masks were transformed to different spaces, nearest-neighbor interpolation was preferred over other interpolation algorithms, such as trilinear and spline interpolation, because otherwise the edges of the masks get smoothed out and mask size can increase arbitrarily.

Preprocessing fMRI data

All data was preprocessed using the FSL FEAT preprocessing pipeline [version 5.09; Smith et al., 2004; Woolrich et al., 2009], as implemented in the NiPype fMRI pipeline framework [create_featreg_preproc(); Gorgolewski et al., 2011]. This pipeline motion-corrects the data using the MCFLIRT algorithm, makes a brain mask in individual functional space using BET, and normalizes the data such that the median voxel intensity within the brain is 10,000. Then, depending on the subsequent analysis, a 1.5 mm full-width-half-maximum (FWHM), a 5.0 mm FWHM, or no Gaussian smoothing kernel was applied. The data were high-pass filtered with a cutoff of 128 seconds. Lastly, the motion parameters obtained by the MCFLIRT algorithm and their first derivatives were used as regressors in a voxelwise general linear model (GLM) to filter out motion-induced noise. The residuals of this GLM were used as input to all further analyses. As an (almost) whole-brain volume was acquired using protocol 3 (see section

"Exploratory voxelwise analyses protocol 3"), these data were corrected for B_0 field inhomogeneities using FSL's FUGUE and the obtained B_0 fieldmaps, before it was submitted to the FEAT preprocessing pipeline. Visual inspection suggested that the influence of this correction was negligible in the subcortex.

fMRI data analysis

Voxelwise tSNR maps of the unsmoothed data were created by taking, for every voxel, its mean intensity across a run, and dividing it by the standard deviation of its intensity across the run. Mean voxelwise tSNR, averaged over all voxels inside a mask, was then extracted for every protocol, participant, run, and ROI.

To investigate whether the decreased tSNR at higher voxel resolutions could be mitigated by the increased number of voxels measured per ROI, we also calculated ROI-wise tSNR. For every ROI-mask, the signal of every voxel inside that mask was averaged, to get a mean ROI signal time course. The ROI-wise tSNR was calculated by dividing the mean intensity of this signal by the standard deviation through time of this signal.

All tSNR measures were calculated on unsmoothed, but otherwise completely preprocessed data. Therefore, the found tSNR values were corrected for, for example, subject movement and slow signal drifts. Furthermore, the signal that was used in the ROI GLM analysis was identical to the signal used to calculate tSNR, enabling us to relate the found tSNR and percent signal change estimates of the GLM to simulation studies of Murphy et al. [2007].

We also deconvolved and visualized the task-locked signal of the ROI signal time courses for different conditions by fitting a GLM with finite impulse regressors [Poldrack et al., 2011] implemented in the Python package pyFIR (version 0.1; https://github.com/Gilles86/pyFIR). This analysis was performed on the mean ROI signal described above, to visually assess the BOLD sensitivity of the different protocols in the different ROIs. Three conditions (go trials, failed stop trials, and successful stop trials) were modeled with each 9 regressors corresponding to offsets of 0, 2, 4, 6, 8, 10, 12, 14, and 16 seconds after task onset. The parameter estimates for the different regressors were averaged across participants and plotted as a function of their offset. For protocols with good BOLD sensitivity, we expected to see a typical hemodynamic response function in all conditions and ROIs, with a peak at around 4–6 seconds. When BOLD sensitivity was sufficient, we expected the estimated height of this peak to be highly significantly different from zero.

We also created an event-related GLM design matrix with canonical HRF regressors using Nipy [0.4.0; Brett et al., 2009]. The design matrix contained three regressors of interest, corresponding to go, failed stop, and successful stop trials. One second block functions at trial onset were convolved with a canonical double-gamma hemodynamic response function (HRF) [Glover, 1999; Worsley and Friston, 1995]. A constant, the first-order derivatives of the HRFs, and a second-order polynomial were also added to the model, to account for individual differences in the hemodynamic responses and slow signal drifts. The GLM was fitted to the ROI-signal time series of every block using GLSAR AR(1) estimation, as implemented in Statsmodels [Seabold and Perktold, 2010], to account for temporal autocorrelation in the signal. For every participant, ROI, protocol, and the mean value of every beta-regressor over the three runs was used as input in a one-sample *t*-test against baseline, or a paired *t*-test between conditions. They were also used as input to a Bayesian *t*-test [Morey and Rouder, 2015] to estimate the Bayes factor (BF) between a model where the different conditions lead to different BOLD responses versus a model where they do not. In contrast to traditional frequentist *P*-values, BFs offer a natural interpretation as the amount of evidence the researcher has for one hypothesis over another, without being biased toward rejecting the null hypothesis [Rouder et al., 2012; Wagenmakers, 2007]. However, there is not a straightforward way to control for the multiple comparisons problem without substantial additional modeling [Neath and Cavanaugh, 2006; Stephens and Balding, 2009]. We therefore chose not to perform multiple comparison correction on the Bayesian analysis, but leave it to the reader to interpret the resulting BF in a cautious manner.

We performed statistical analyses both on the entire samples of protocol 1–4 (with 5, 5, 20, and 10 subjects, respectively), as well as on a subset of five subjects, to keep the number of subjects equal over the (analysis of) the four protocols.

T_2* Estimation

To obtain an empirical estimate of the T_2* relaxation values of the different BG nuclei at both 3 T and 7 T MRI, an exponential decay function was fitted to the signal intensities at different echo times of the FLASH sequence images (see section above on "Structural MRI"). This estimate was calculated using voxelwise Ordinary Least Squares (OLS) regression in log-space [Lutti et al., 2014; Weiskopf et al., 2014]. We opted not to use robust regression since the number of data points was too limited to do this effectively (3 and 4, respectively) and the young and healthy participants of this study were specifically selected for minimal movement during scanning. The voxelwise estimates were subsequently extracted and averaged within the anatomical masks of the nuclei-of-interest.

Exploratory Voxelwise Analyses Protocol 3

After performing the analysis described in section "fMRI data analysis", only protocol 3 turned out to have sufficient BOLD sensitivity in the BG ROI. Therefore, we also performed a voxelwise analysis on the data resulting from protocol 3, but not the other protocols, in both subcortex and cortex. Ideally, the protocol should have sufficient sensitivity in both cortical (although TE was not optimal for cortex) and subcortical regions to test task-related activations. To investigate the sensitivity in cortical areas, we

TABLE III. Mean values of behavioral measures per sequence

Behavioral measure	Protocol 1	Protocol 2	Protocol 3	Protocol 4
Median correct Go RT (ms)	420.3 (43.3)	440.5 (61.9)	477.2 (97.9)	531.5 (128.3)
Median failed stop RT (ms)	387.5 (29.8)	407.9 (54.8)	438.0 (79.5)	490.1 (120.1)
Percentage go discrimination errors	0.07 (0.16)	0.30 (0.30)	0.36 (0.43)	0.29 (0.70)
Mean SSD (ms)	200.3 (46.7)	204.6 (91.8)	247.2 (91.0)	317.0 (122.1)
Percentage successful inhibition	52.6 (3.0)	51.2 (6.3)	56.1 (6.4)	58.1 (6.8)
Mean SSRT (ms)	215.3 (31.6)	231.4 (71.2)	211.8 (33.2)	192.7 (25.9)

used a conventional group-level voxelwise analysis in MNI152 space. To address possible subcortical activations outside of the a-priori selected ROIs, we also used a custom groupwise template with high contrast in subcortex.

To investigate the BOLD sensitivity of protocol 3 in MNI152 space, the mean functional images of protocol 3 were registered to the uniform T_1 weighted image of the whole-brain MP2RAGE, using linear affine registration as implemented in ANTS [version 2.0.0; Avants et al., 2009]. The T_1 weighted images were brain-extracted using the brain mask created by the FSL BET-algorithm applied to the INV2-image [Smith, 2002], and then registered to the 1 mm isotropic MNI152 standard brain using non-linear registration via the SyN-algorithm, as implemented in ANTS [version 2.0.0; Avants et al., 2009]. The combined transform of these two transformations (from the mean EPI to T_1-weighted anatomical image and from T_1-weighted anatomical image to 1 mm isotropic MNI152 standard brain) was used to transform the statistical parametric maps in individual space to MNI152 standard space using nearest-neighbor interpolation.

Preferably, the fMRI data can be transformed to a space where voxels originating from a particular anatomical location in one individual (e.g., the subthalamic nucleus of participant 1) have a very high overlap with voxels from other individuals originating from the same anatomical location (e.g., the subthalamic nucleus of participant 2). As, the individual T_1-weighted images have little tissue contrast in subcortex, which hampers the anatomical overlap between functional EPI data and a standard template in this region, in addition a study-specific group T_2*-weighted FLASH template was created by non-linearly registering (using the SyN-algorithm implemented in ANTS) all the individual T_2* weighted FLASH images (middle echo time of 20.39 ms) to the FLASH image of the first participant, and then iteratively registering all anatomical images to the mean image of all individual transformed images. After five iterations, the mean of the transformed images did not considerably change anymore. The mean of these images showed very high contrast in the subcortex, and the different nuclei-of-interest are clearly visible.

The functional images of protocol 3 were, in addition to the MNI152 space, also registered to this group FLASH space, to investigate the topology of activation clusters in the subcortex with high anatomical specificity without constraining the analysis to a-priori selected ROIs.

A voxelwise GLM group analysis was performed both in the study-specific 0.5 mm T_2* weighted FLASH space, as well as in 1 mm standard MNI152 space. The data was smoothed with either a 1.5 mm (for the study-specific template analysis) or 5.0 mm (for MNI152 1mm space) FWHM Gaussian smoothing kernel. Go, failed stop, and successful stop trials were modeled as separate conditions. First-order derivatives of the canonical HRF were included as nuisance regressors. The estimated contrasts were: (1) successful stop–go, (2) failed stop–go, (3) successful stop–failed stop, (4) failed stop–successful stop. A mixed-effects level 2 analysis was performed using FSL's FLAME1. For the analysis in MNI152-space, multiple comparison correction was performed using Gaussian Random Field (GRF) Theory, as implemented in FSL's *smoothestimate* and *cluster*, using a voxelwise threshold of $z > 3.1$ and GRF cluster-threshold of $P < 0.05$. For the analysis in the group template space, we believed the assumption of a Gaussian random field was not tenable, because the smoothing of the data had been very limited. Therefore, for this analysis, we opted for a voxelwise false discovery rate (FDR) correction (*fdr*-function of FSL, $q < 0.05$).

Exploratory Connectivity Analyses

An exploratory connectivity analysis was conducted to test whether the different protocols were capable of recovering functional connectivity patterns in the BG. In this connectivity analysis, a correlation matrix representing the correlations between the measured signals of the different BG nuclei was computed. The inputs of the correlation matrix were the preprocessed mean ROI timeseries (task-related activity was not modeled here). If BOLD sensitivity and specificity were high, we would expect to see high connectivity between homologous BG nuclei across the two hemispheres (e.g., a high correlation between left and right STN), preferably more so than between spatially closer, but functionally distinct nuclei (e.g., left STN and left SN).

RESULTS

Behavior

The median correct go RT and the estimate of the SSRT in all experiments were typical for young adults [Aron, 2006], and the inhibition rates were close to 50% (see Table III). As expected, median RTs of failed stops were faster than

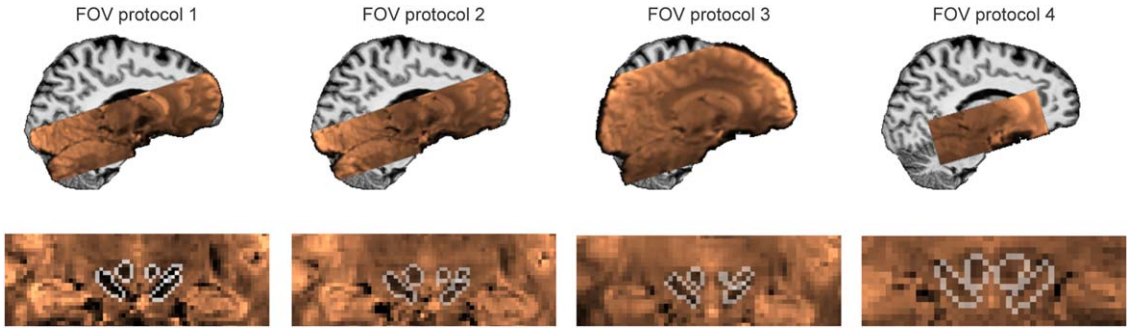

Figure 2.

Illustration of the Field-of-views of the four protocols and anatomical masks. The top row shows, for a representative subject, a sagittal slice of the mean functional images overlaid on the T1-weighted anatomical image. The bottom row shows the outlines of the individual masks for RN, STN, and SN, overlaid on coronal slices of the mean functional image (radiological convention). The coronal slices are chosen such that they correspond to the center-of-mass of the right SN mask. [Color figure can be viewed at wileyonlinelibrary.com]

correct go trials, and inhibition rate was around 50%. Median go RTs were not correlated with SSRTs, in line with the independence assumption of the race model [Aron, 2006; Logan and Cowan, 1984; see also Shenoy and Yu, 2011].

Transformation of Anatomical Masks

The transformation of the anatomical masks from the 7 T-FLASH-space to the four functional spaces was visually inspected for all participants. A representative example of the individual anatomical masks transformed to individual space for the four protocols can be found in Figure 2.

The volumes of the anatomical masks and the between-rater agreement, as indicated by the Dice-coefficient [Dice, 1945], can be found in Table IV.

T_2* Estimates

At 3 T, the T_2* relaxation value in the left STN was on average 34.2 ms (std 6.7) and 35.6 ms in right STN (std 6.8). This is considerably lower than the 66 ms, the approximate T_2* relaxation value for cortex at 3 T [Peters et al., 2007 see Table IV for the T2*-estimates for the different nuclei].

As expected, the T_2* value in the BG is even shorter at 7 T, on average 15.2 ms (std. 1.7) in the left STN and 14.9 ms (std. 2.0) in the right STN, as compared with approximately 33 ms in cortex [Peters et al., 2007]. This confirms that, especially at 7 T, functional protocols that are optimized to functional imaging of the cortex might have too long echo times to have robust BOLD sensitivity in iron-rich subcortical nuclei, such as the BG.

tSNR

Voxelwise temporal signal-to-noise ratios were extremely low for protocol 1 (1.2 mm/TE = 22 ms/7 T), 2 (1.2 mm/15 ms/7 T), and 4 (1.5 mm/30 ms/3 T). For left/right STN, tSNR was 8.2 (std 0.8)/8.3 (1.2) for protocol 1, 12.4 (0.9)/12.8 (1.6) for protocol 2, and 9.2 (1.0)/9.2 (1.3) for protocol 4. Temporal SNR in other BG nuclei was comparable (see Fig. 3). Earlier simulation studies

TABLE IV. Mean and standard deviations of inter-rater consistency (Dice coefficient) and anatomical mask sizes (mm^3)

	Dice	Volume (mm^3)
STN_L	0.73 (0.16)	54 (13)
STN_R	0.74 (0.14)	58 (12)
SN_L	0.79 (0.07)	297 (123)
SN_R	0.77 (0.05)	298 (129)
RN_L	0.89 (0.03)	269 (44)
RN_R	0.89 (0.02)	261 (46)
GPi_L	0.80 (0.05)	367 (79)
GPi_R	0.81 (0.06)	357 (71)
GPe_L	0.86 (0.03)	1020 (156)
GPe_R	0.86 (0.04)	958 (146)

TABLE V. Estimated T_2* relaxation values at 3 T and 7 T

	T2* at 3 T in ms (std)	T2* at 7 T in ms (std)
mask		
STN_L	34.2 (6.7)	15.2 (1.7)
STN_R	35.6 (6.8)	14.9 (2.0)
SN_L	36.6 (4.3)	14.1 (1.7)
SN_R	36.6 (10.0)	13.8 (1.4)
RN_L	42.4 (5.0)	16.9 (1.5)
RN_R	40.1 (3.9)	16.9 (1.5)
GPi_L	34.3 (2.1)	13.1 (1.3)
GPi_R	34.4 (2.0)	12.8 (0.8)
GPe_L	31.8 (2.4)	13.1 (1.2)
GPe_R	32.4 (2.7)	12.9 (0.9)

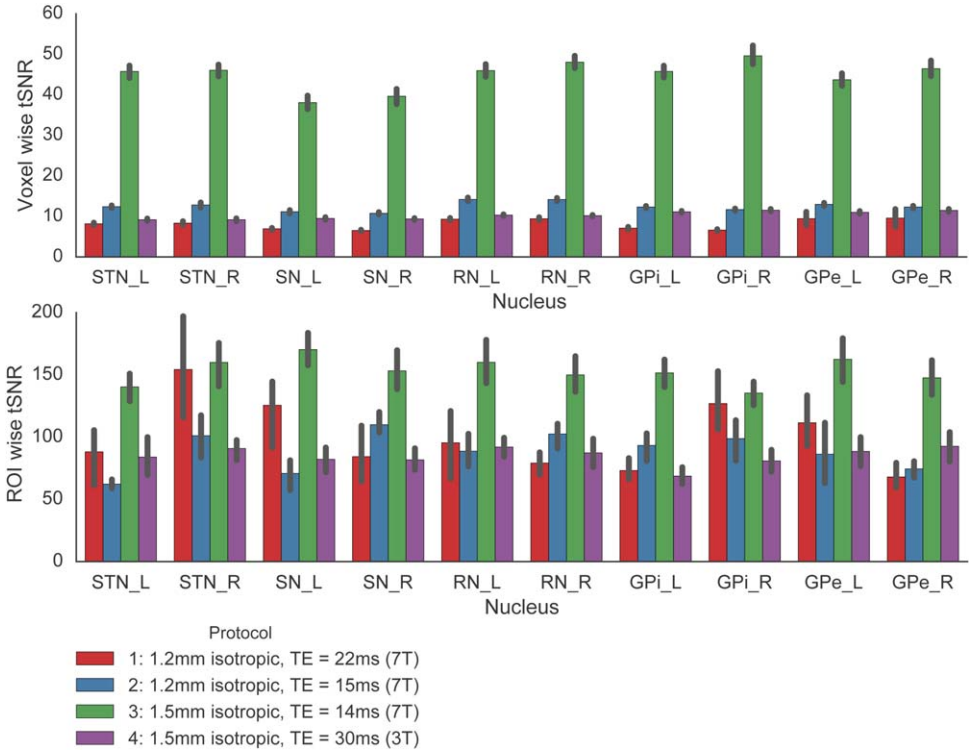

Figure 3.

Voxel- (top) and ROI-wise (bottom) temporal signal-to-noise ratios (tSNR) in the basal ganglia for the four protocols. Error bars represent bootstrapped 67% confidence interval. [Color figure can be viewed at wileyonlinelibrary.com]

suggest that a tSNR in these ranges makes it virtually impossible to detect activations patterns in the individual brain within an acceptable scan time [Murphy et al., 2007].

Protocol 2 showed a significantly higher tSNR than protocol 1 ($t(4) = 13.6$, $P = 0.0002$ for left STN and $t(4) = 7.7$, $P = 0.002$ for right STN), suggesting that the reduction of TE indeed increases the tSNR.

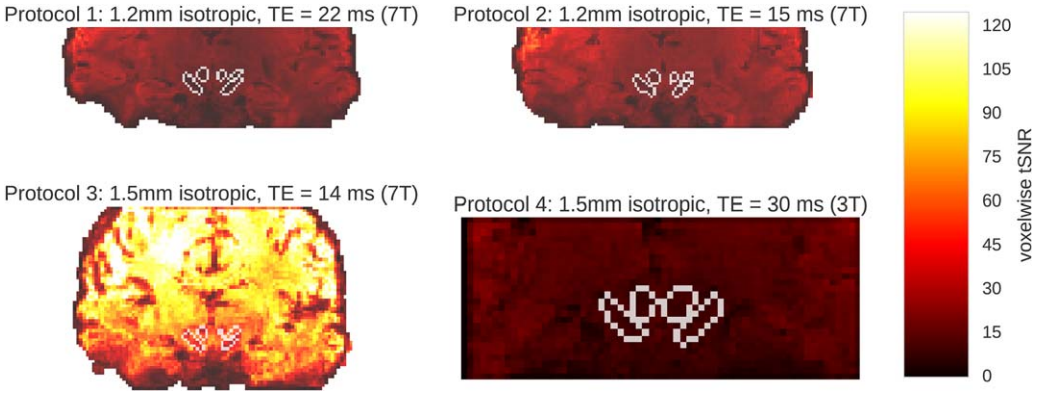

Figure 4.

Coronal slices of the voxelwise tSNR-maps for the four protocols in a representative subject. The coronal slices are chosen such that they correspond to the center-of-mass of the right SN mask. [Color figure can be viewed at wileyonlinelibrary.com]

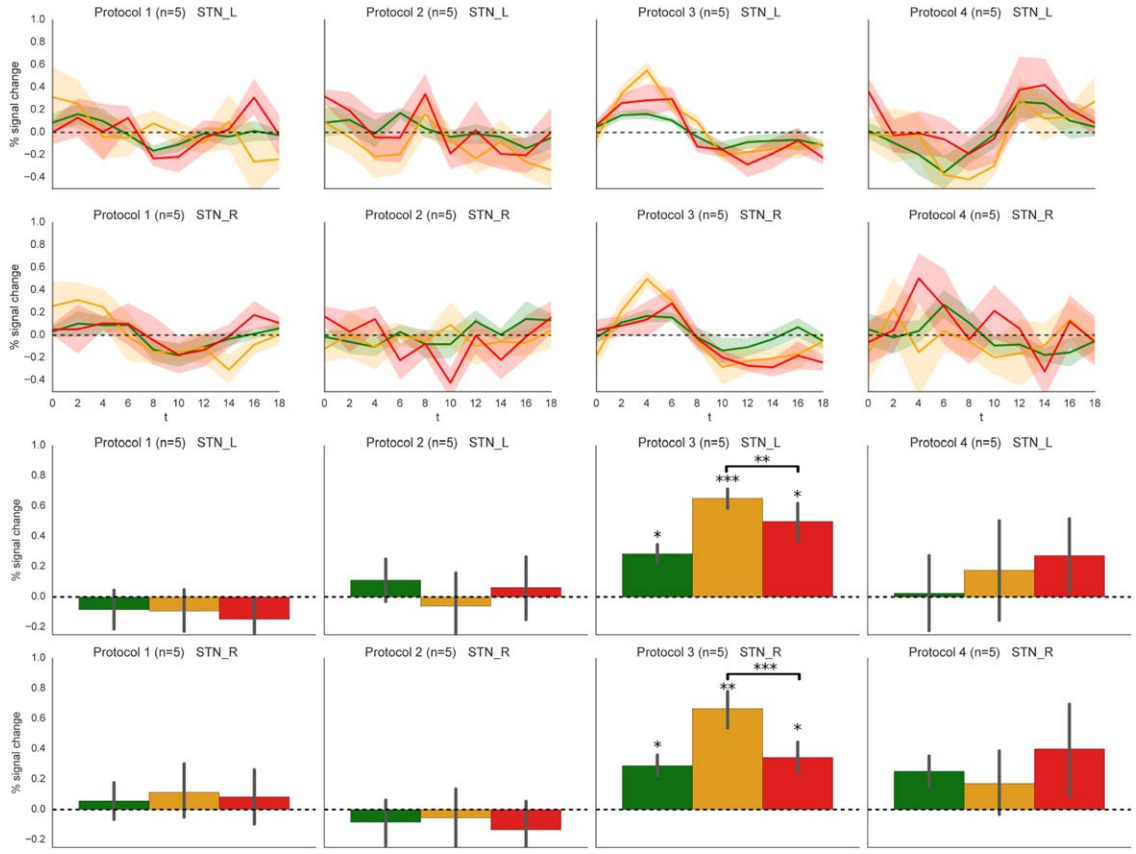

Figure 5.

Raw task-locked mean time series (top) and corresponding GLM parameter estimates (bottom) for all four protocols in left and right STN for five subjects. For protocol 1–3 all five subjects are overlapping. For protocol 4, four out of five subjects are overlapping. Shaded area and error bars indicate 67% bootstrapped confidence interval, corresponding to the standard error of the mean (SEM). Green corresponds to go trials, orange to failed stop trials, and red to successful stop trials. Only for protocol 3 are any parameters significantly different from zero after FDR correction. ($q < 0.05$). * = $P < 0.05$, ** = $P < 0.01$, *** = $P < 0.001$. [Color figure can be viewed at wileyonlinelibrary.com]

Only protocol 3 (1.5 mm/14 ms/7 T) showed an acceptable tSNR: 48.6 (11.1) for left STN, and 50.5 (11.1) for right STN, see also Figure 3 (top). Temporal SNR in such a range should allow for detecting neural activation in the individual brain in a reasonable amount of time [Murphy et al., 2007].

Higher spatial resolutions always lead to decreased tSNR but also to smaller partial volume effects. Furthermore, as the tSNR can be increased by spatial averaging the temporal SNR of the mean time series per ROI was also calculated. This showed that the ROI-wise tSNR is still highest for protocol 3 (140.3, (std. 57.2) for left STN, 160, (91.7) for right STN). But, as expected, protocol 1 (88.2 (47.4) for left STN, 154.3 (47.5) for right STN) and 2 (62.3 (12.0) for left STN, 101.1 (39.9) for right STN) show tSNRs that are closer to that of protocol 3 when the signal is averaged over all voxels (see also Fig. 3, bottom). This suggests that most of the noise was uncorrelated across voxels, and most likely consists of image noise, rather than physiological noise [Triantafyllou et al., 2006].

Four representative coronal slices of the tSNR maps are depicted in Figure 4. They clearly show the improved tSNR in protocol 3 (1.5 mm/14 ms/7 T), as well as the relative drop in tSNR in the subcortex as compared with cortex at 7 T, especially in protocol 1 (1.2 mm/22 ms/7 T) and 2 (1.2 mm/15 ms/7 T), which had a relatively high acceleration factor (see Table I).

Task-Locked ROI Analyses

Finite impulse response (FIR)-analysis

To keep things concise and easy to compare, for the FIR and traditional GLM, we report analyses on the same five subjects in protocol 1, 2, and 3, and five subjects in protocol 4, of which four subjects overlap with protocol 1–3

TABLE VI. Frequentist and Bayesian statistics for main task contrasts using protocol 3

	Successful stop > go		Failed stop> go		Failed stop> successful stop	
	frequentist	BF10	frequentist	BF10	frequentist	BF10
GPe_L	$t(19) = -1.52$, $P = 0.144$	0.63	$t(19) = 1.40$, $P = 0.176$	0.54	$t(19) = 3.36$, $P = 0.003$*	13
GPe_R	$t(19) = 0.57$, $P = 0.577$	0.27	$t(19) = 3.08$, $P = 0.006$*	7.63	$t(19) = 2.58$, $P = 0.018$*	3.12
GPi_L	$t(19) = -1.13$, $P = 0.271$	0.41	$t(19) = 0.55$, $P = 0.591$	0.27	$t(19) = 1.14$, $P = 0.267$	0.41
GPi_R	$t(19) = -1.42$, $P = 0.173$	0.55	$t(19) = 0.74$, $P = 0.466$	0.3	$t(19) = 1.68$, $P = 0.110$	0.76
RN_L	$t(19) = 1.57$, $P = 0.132$	0.67	$t(19) = 4.66$, p<.001*	173	$t(19) = 2.38$, $P = 0.028$*	2.2
RN_R	$t(19) = 1.16$, $P = 0.260$	0.42	$t(19) = 5.22$, p<.001*	531	$t(19) = 3.70$, $P = 0.002$*	25
SN_L	$t(19) = 0.83$, $P = 0.416$	0.32	$t(19) = 3.26$, $P = 0.004$*	11	$t(19) = 1.93$, $P = 0.069$	1.08
SN_R	$t(19) = 1.26$, $P = 0.224$	0.46	$t(19) = 5.72$, p<.001*	1423	$t(19) = 2.38$, $P = 0.028$*	2.19
STN_L	$t(19) = 1.48$, $P = 0.154$	0.6	$t(19) = 4.29$, p<.001*	82	$t(19) = 2.95$, $P = 0.008$*	6.05
STN_R	$t(19) = -0.87$, $P = 0.394$	0.33	$t(19) = 3.35$, $P = 0.003$*	13	$t(19) = 3.18$, $P = 0.005$*	9.23

A Bayes factor (BF10) larger than 1 means evidence for an effect, a Bayes factor less small 1 means evidence in favor of no effect. See also Figure 6 and Supporting Information Tables S1 and S2. * = significant effect after FDR-correction ($q < 0.05$).

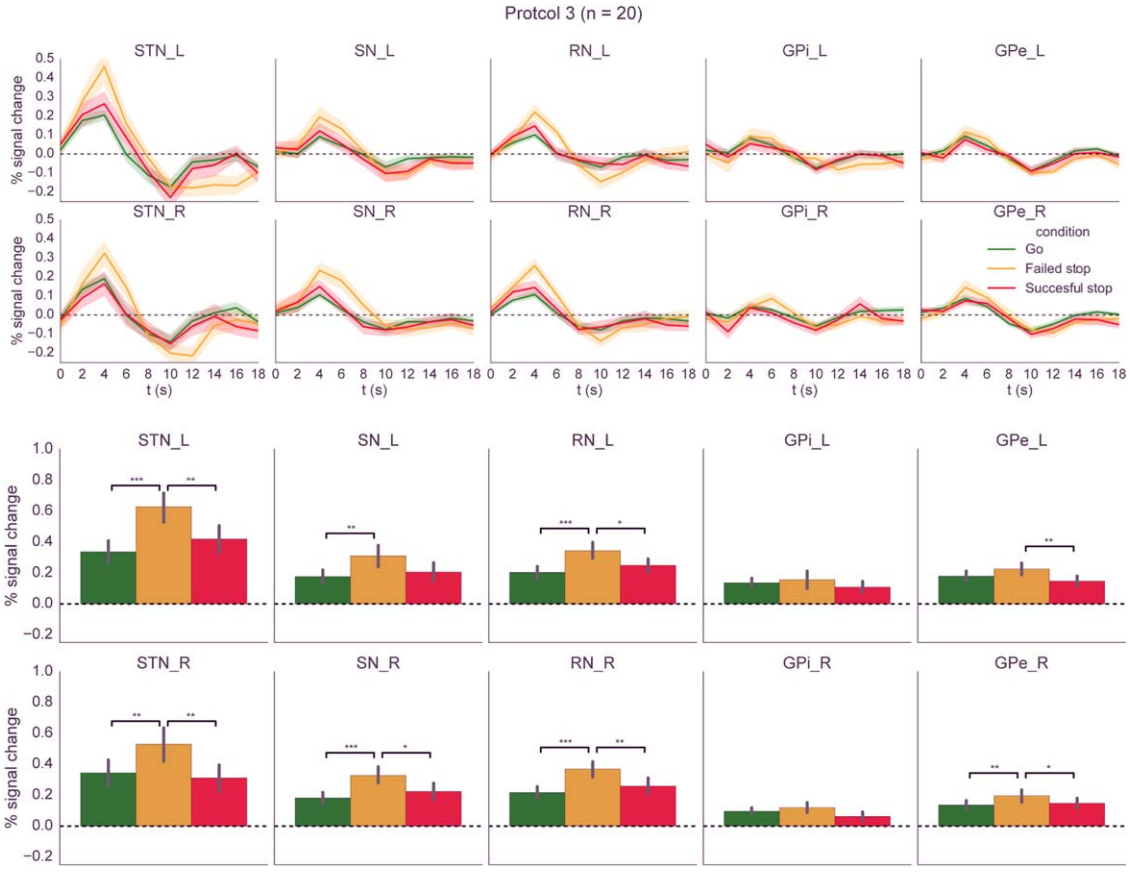

Figure 6.

Raw task-locked mean time series (top) and corresponding GLM parameter estimates (bottom) for protocol 3 across all basal ganglia masks for 20 subjects. Shaded area and error bars indicate 67% bootstrapped confidence interval, corresponding to the standard error of the mean (SEM). Green corresponds to go trials, orange to failed stop trials, and red to successful stop trials. * = $P < 0.05$, ** = $P < 0.01$, *** = $P < 0.001$. [Color figure can be viewed at wileyonlinelibrary.com]

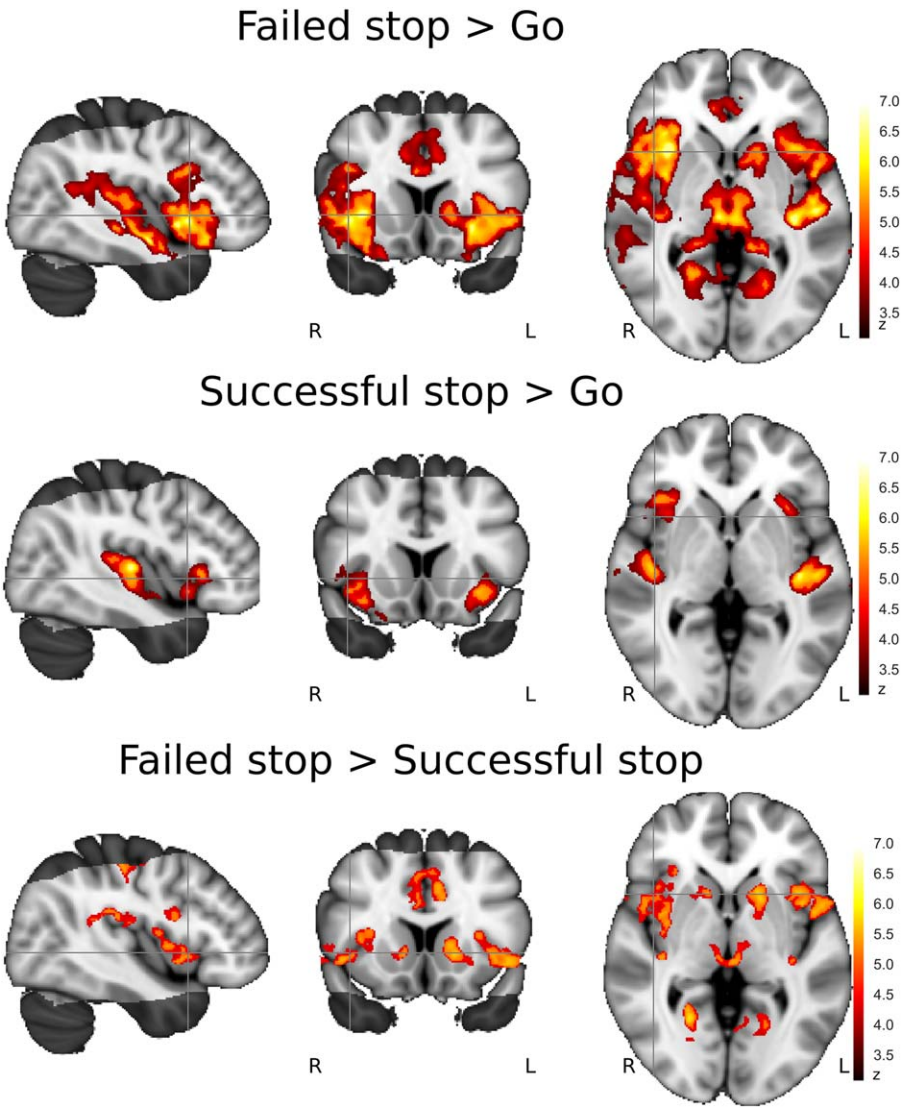

Figure 7.

Whole-slab SPMs for main task contrasts in protocol 3. From left to right: sagittal (MNI152 $X = 43$), coronal (MNI152 $Y = 14$), and axial (MNI152 $Z = 0$) slices. Parts of the MNI brain that did not overlap with the functional data of all 20 participants were not included in the statistical tests and are darkly shaded. [Color figure can be viewed at wileyonlinelibrary.com]

(specifically, group A and B for protocols 1–3, and group A and a randomly picked participant of group C for protocol 4; see Table II).

Qualitative inspection of the task-locked ROI time series suggested that protocol 1 (1.2 mm/22 ms/7 T), 2 (1.2 mm/15 ms/7 T), and 4 (1.5 mm/30 ms/3 T) show no robust task-related BOLD responses in left or right STN (see the top panel of Fig. 5). They lack the prototypical HRF pattern of a peak at 4–6 seconds after task onset. Such a pattern was, in contrast, clearly present in the STN timeseries of protocol 3, already with five subjects (Fig. 5, top panel; see also Supporting Information Materials S3). This suggests that the higher tSNR in protocol 3 also leads to robust BOLD sensitivity.

ROI GLM

For protocol 1 (1.2 mm/22 ms/7 T) and 2 (1.2 mm/15 ms/7 T), no parameter estimates were significantly different from 0 after FDR correction (all $P > 0.05$, see Fig. 5 and Supporting Information materials S1 for additional statistics). All Bayes Factors suggested anecdotal evidence for the null hypothesis (BF10 range 0.42–1.02). This suggests that there was no reliable task-related BOLD activity

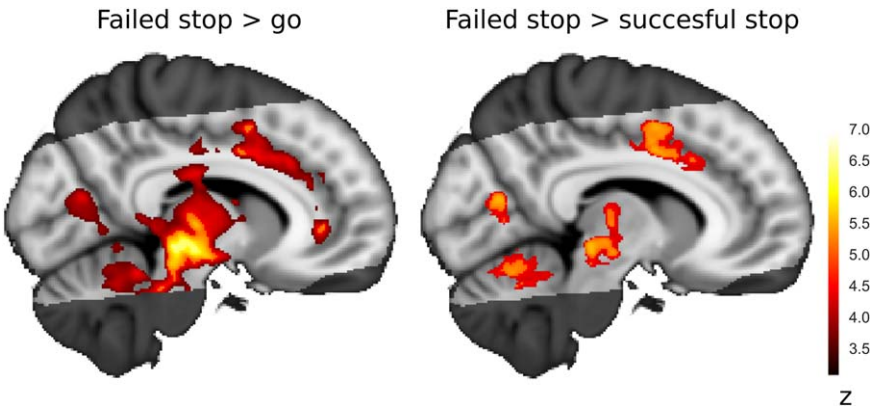

Figure 8.

Sagittal slices (MNI152 $X = 9$) of two contrasts that show extensive activated clusters across the subcortex and brainstem for protocol 3. This illustrates the lack of anatomical specificity of conventional voxelwise GLM with moderate (5.0 mm FWHM) smoothing. [Color figure can be viewed at wileyonlinelibrary.com]

detected in any of the conditions. Accordingly, there were also no significant differences between the task conditions in any of the nuclei (see Supporting Information Material S2 for details).

For protocol 3 (1.5 mm/14 ms/7 T), all three parameters estimates were significantly different from zero in both left and right STN, as shown by *t*-tests (all $P < 0.05$, FDR corrected; Bayesian t-tests showed Bayes factors in favor of an effect, BF10 range 4–784; see also Fig. 5 and Supporting Information material S1). In other words: in both left and right STN, and in every condition, after task-onset there was a significant BOLD response, detected already with five subjects. Also, the contrast "failed stop" > "go" was significant in both left and right STN in five subjects ($t(4) = 8.3$, $P = 0.0011$ for left STN, BF10 = 34, $t(4) = 9.17$, $P = 0.0008$, BF10 = 45 for right STN).

For protocol 4 (1.5 mm/30 ms/3 T), using five subjects (all four subject of group A and a randomly selected participant of group C; see Table II), and after FDR correction, no parameter estimates were significantly different from zero according to *t*-tests.

Bayes Factors were in the range of 0.40–2.75, where all Bayes Factors showed evidence for the null hypothesis, except for the "go"-condition in the right STN. No contrasts between conditions were significant.

When all 20 subjects were included for protocol 3 (1.5 mm/14 ms/7 T), similar patterns were found, albeit with more robust *P*-values and Bayes Factors. All nuclei except for the left and right GPi and left GPe showed a higher BOLD response during failed stop trials compared with go trials (FDR corrected; see also Table VI and Fig. 6). Also, left and right STN, right SN, the left and right RN, and left and right GPe showed a higher BOLD response during failed stops than successful stop trials. None of the nuclei showed a larger activation for successful stop trials than for go trials (see also Supporting Information Table S2).

When all 10 subjects were included for protocol 4, after FDR correction, none of the parameter estimates were significantly different from zero. However, Bayesian *t*-tests suggested evidence in favor of a model where BOLD activity was different from baseline for left STN (successful stop; $BF_{10} = 2.49$), right STN (go trials; $BF_{10} = 16.00$; failed stops; $BF_{10} = 3.16$), left GPi (failed stops; $BF_{10} = 1.14$), and right RN (failed stops; $BF_{10} = 3.45$; see also Supporting Information Material S1 and S3). However, no significant differences between conditions were found (all $P > 0.05$, BF10 in range 0.4–1; see also Supporting Information Material S2 and S3).

Voxelwise analysis MNI152-space (protocol 3)

We computed a voxelwise GLM analysis only on the data of protocol 3 (1.5 mm/14 ms/7 T), since only this protocol showed robust BOLD sensitivity in the BG, and, importantly, only this protocol allowed for scanning the majority of cortex and could potentially be used to investigate cortico-subcortical interactions. For these analyses, all 20 subjects were included.

For the "failed stop > go" contrast, many significant activation clusters were found in cortex and subcortex in both hemispheres. These include inferior frontal gyrus (pars operculum, IFG), pre- Supporting Information motor (pre-SMA), anterior cingulate cortex (ACC), early visual cortex (V1, V2), the middle and superior temporal gyrus, primary auditory cortex, insular cortex, and two clusters that covered almost the entire subcortex and brainstem bilaterally (see Fig. 7, top; Fig. 8; top; Table VIIa).

The "failed stop > successful stop" contrast also showed a very large set of significant activation clusters across cortex and subcortex, where, again, the subcortical clusters were very large and showed little anatomical specificity (see Figs. 7 and 8 and Table VIIb).

For the "successful stop > go" contrast, the spread of significant activation clusters is much sparser. Only the

TABLE VII. Significant clusters of the whole-slab voxelwise GLM analysis on protocol 3 for three main contrasts (failed stop > go, successful stop > go, and failed stop > successful stop)

Name	MNI X	MNI Y	MNI Z	Volume (mm^3)	Max z-value
(a) Failed stop > Go					
Left insular cortex/subcortex/brainstem	−40	−6	−11	34,321	6.79
Right insular cortex/subcortex/brainstem	32	17	−7	27,849	6.44
Anterior cingulate cortex (ACC)	−3	23	23	3,014	5.15
Right primary visual cortex (V1)	23	54	−2	1,476	5.41
Left primary visual cortex (V1)	−19	−61	2	700	4.67
Left posterior cingulate cortex (PCC)	−11	−18	39	638	5.04
Pre-supplementary motor Area (pre-SMA)	6	7	45	532	4.74
Left middle temporal gyrus (MTG)	44	−28	−7	440	5.44
Left posterior cingulate gyrus	−13	−39	−2	417	4.97
Right superior temporal gyrus (STG)	63	2	2	347	5.15
Right posterior cingulate cortex (PCC)	5	−15	25	155	4.47
Right anterior cingulate cortex (ACC)	7	42	1	80	4.67
Right middle temporal gyrus (MTG)	54	−59	6	71	4.45
Left insular cortex	−32	−19	18	69	4.28
Right cerebellum	9	−43	−18	69	4.24
Left temporal pole	−46	2	−18	44	4.68
Left anterior cingulate cortex (ACC)	−6	37	7	42	4.37
Right anterior cingulate cortex (ACC)	4	38	12	41	4.22
(b) Failed stop > successful stop					
Left posterior cingulate cortex (PCC)	−11	−17	38	9,931	5.32
Right inferior fronal cortex/frontal operculum (IFG)	47	2	5	8,837	5.39
Left striatum	−14	12	2	7,879	5.36
Left cerebellum	−25	−59	−23	7,221	5.23
Subcortex/brain stem	8	−25	−6	6,229	5.3
Left primary motor cortex (M1)	−38	−25	52	4,186	5.46
Right primary auditory cortex	34	−31	18	3,957	5.33
Left primary auditory cortex	−50	−20	17	3,292	5.75
Right primary visual cortex (V1)	23	−56	0	2,561	5.46
Left primary visual cortex (V1)	−12	−73	11	1,689	4.83
Right primary motor cortex (M1)	41	−25	50	915	4.97
Left insular cortex	−31	−24	8	449	4.66
Right primary somatosensory cortex/motor cortex (M1/S1)	57	−13	44	369	5.04
Right primary somatosensory cortex/motor cortex (M1/S1)	55	−3	42	320	5
(c) Successful stop > go					
Left primary auditory cortex	−50	−25	7	14,226	6.29
Right primary auditory cortex	44	−17	5	12,266	6.15
Right insular cortex	32	21	−10	6,115	5.09
Left insular cortex	−31	17	−7	3,792	5.44
Right striatum	12	15	0	276	4.82

The contrast successful stop > failed stop showed no significant activation clusters. MNI-coordinates are those of the voxel with the highest z-score.

left and right primary auditory cortex and left and right insula show a significant activation pattern, which is to be expected as there was an auditory stop signal (see Fig. 9, middle row; Table VIIc).

For the "successful stop > failed stop" contrast, no significant activation clusters were found.

Voxelwise analysis on T2-weighted group template*

The registration to the MNI152-standard brain via the T_1-weighted images and the 5.0 mm FWHM smoothing does not allow for high anatomical specificity in the BG. The T_1-weighted images show only little anatomical detail in the subcortex, which causes the registration to standard space to rely mostly on cortical structures. The extensive smoothing might obfuscate small activation clusters by introducing perturbing noise from adjacent areas that are not involved in the task, as well as erroneously join distinct clusters together [Stelzer, 2014].

Therefore, we also created a group-specific T_2*-weighted template at a resolution of 0.5 mm by iteratively registering the individual FLASH images toward each other and repeated the group-level analysis in this space. This template has much higher anatomical contrast in the

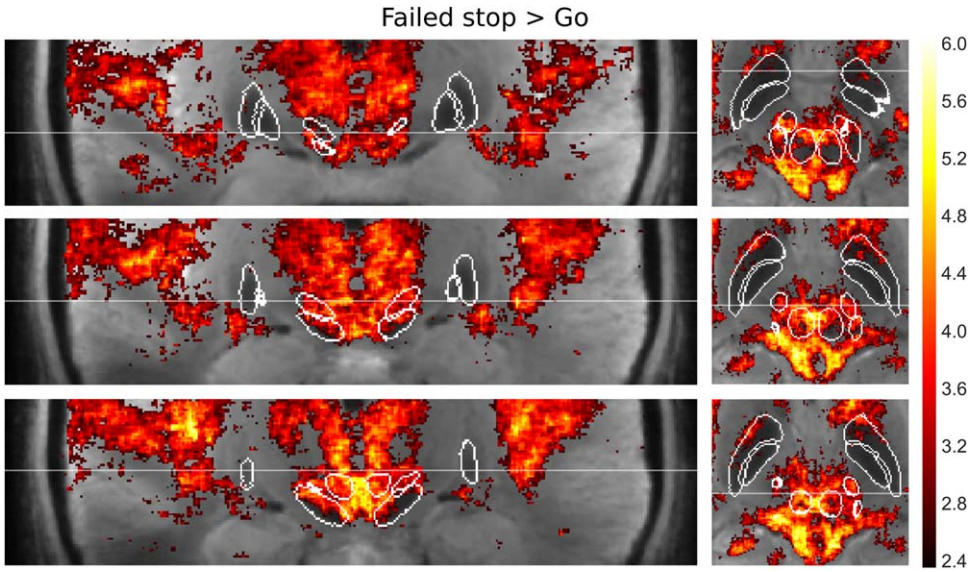

Figure 9.

Slices of the voxelwise analysis of the "**Failed stop > Go**" contrast in the T_2* weighted group template (no MNI152 coordinates) for protocol 3, showing both average anatomy and a SPM of the z-values. Outlines of the anatomical masks are overlaid in white. These masks indicate the area that corresponds to voxels that have been labeled as the nucleus-of-interest nucleus in at least 18 out of 20 participants. The two lateral nuclei are the Globus Pallidus interna (GPi, medial) and externa (GPe, lateral), the most-medial, sphere-like areas are the red nuclei (RN). These lie just dorsal of the substantia nigra (SN), and slightly posterior to the subthalamic nucleus (STN). [Color figure can be viewed at wileyonlinelibrary.com]

subcortex. Also, we used only limited smoothing (1.5 mm FWHM).

This analysis showed, comparable to the MNI152-analysis, extensive activation clusters in the inferior parts of the brain for the "failed stop > go" (Figure 9) contrast, extending well outside the border of the STN, SN, and RN. We found a large cluster immediately dorsal to the STN and RN, probably reflecting the involvement of thalamic nuclei. We also found a cluster medial of the SN and ventral of the RN, which could be attributed to the ventral tegmental area [VTA; Eapen et al., 2011], an important dopaminergic nucleus [Arsenault et al., 2014; Haber, 2014]. The cluster posterior to the RN might be attributed to a number of nuclei in the brainstem, such as the locus coereleus, an important neuromodulatory node [Keren et al., 2015], or the periaqueductal gray [Linnman et al., 2012], among others.

The "failed stop > successful stop" (Figure 10) contrast shows very comparable clusters to the "failed stop > go" contrast, but they are less extensive and have lower *z*-values. This suggest that maybe very similar networks are involved, albeit less heavily.

The activation clusters in the "successful stop > go" (Figure 11) contrast are, comparable to the MNI152-analysis, and show little activation in the subcortex or brainstem. Still, a set of clusters in the thalamus and VTA survived the FDR correction. However, they have the size of only a few voxels and relatively low *z*-values, so a cautious interpretation is warranted.

Connectivity Analyses

Since the specificity of task activation patterns of the different BG nuclei was rather limited, we also investigated node-to-node functional connectivity. If the anatomical masks would correspond to distinct functional signals, they should show clear correlational patterns with higher correlations for functional homologous nuclei across the hemispheres, compared with functionally different nuclei in the same hemisphere. Subcortex BG node-to-node signal correlations were computed, without additional modeling of task-related activity. For the 7 T protocols 1–3 (1.2 mm/22 ms/7 T; 1.2 mm/15 ms/7 T; 1.5 mm/14 ms/7 T), but not the 3 T protocol 4 (1.5 mm/30 ms/3 T), robust correlation patterns were found. Importantly, correlations between contralateral functional homologous nodes tended to be higher compared with functionally distinct nodes that were spatially closer. For example, for protocol 3 (1.5 mm/14 ms/7 T), the correlations between left and right STN (mean $r = 0.52$. std. 0.15) and left and right SN (mean $r = 0.54$, std. 0.14), were on average considerably higher than those between left STN and left SN (mean $r = 0.28$, std. 0.22; $t(19) = 4.9$, $P < 0.001$ and $t(19) = 5.3$, $P < 0.001$) and right STN and right SN (mean $r = 0.34$, std. 0.2; $t(19) = 3.2$, $P < 0.001$ and $t(19) = 4.3$, $P < 0.001$). These correlational patterns suggest that these connectivity measures adhere to functional anatomy and are not just an artifact of spatially correlated noise.

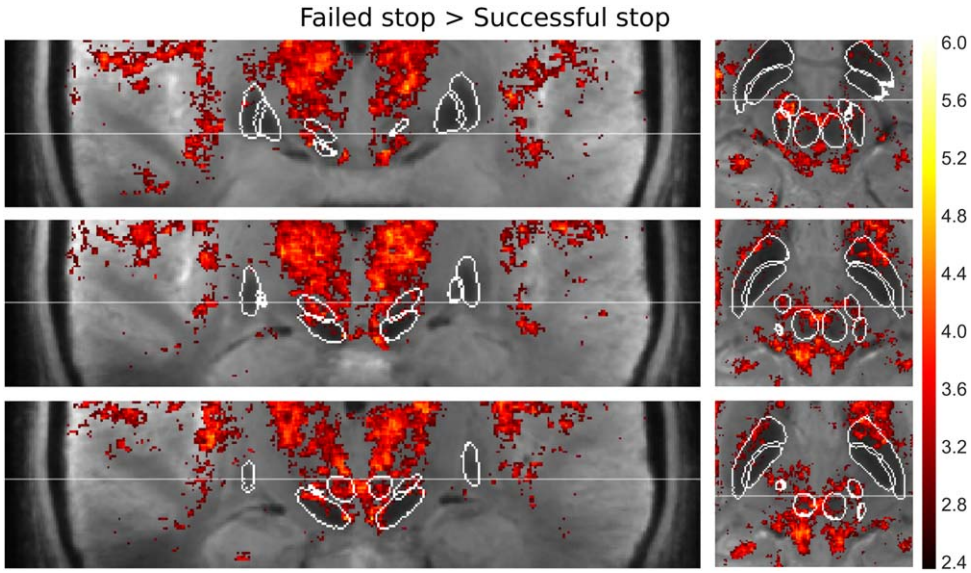

Figure 10.

Slices of the voxelwise analysis of the "**Failed stop > Successful stop**" contrast in the T_2* weighted group template for protocol 3, showing both average anatomy and a SPM of the z-values. Outlines of the anatomical masks are overlaid in white. These masks indicate the area that corresponds to voxels that have been labeled as the nucleus-of-interest nucleus in at least 18 out of 20 participants. The two lateral nuclei are the Globus Pallidus interna (GPi, medial) and externa (GPe, lateral), the most-medial, sphere-like areas are the red nuclei (RN). These lie just dorsal of the substantia nigra (SN), and slightly posterior to the subthalamic nucleus (STN). [Color figure can be viewed at wileyonlinelibrary.com]

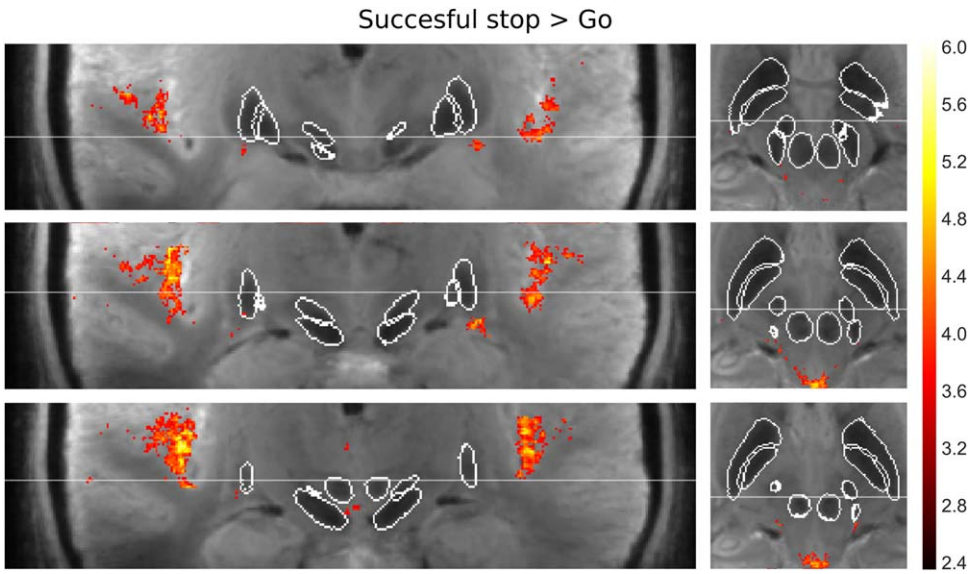

Figure 11.

Slices of the voxelwise analysis of the "**Successful stop > Go**" contrast in the T_2* weighted group template for protocol 3, showing both average anatomy and a SPM of the z-values. Outlines of the anatomical masks are overlaid in white. These masks indicate the area that corresponds to voxels that have been labeled as the nucleus-of-interest nucleus in at least 18 out of 20 participants. The two lateral nuclei are the Globus Pallidus interna (GPi, medial) and externa (GPe, lateral), the most-medial, sphere-like areas are the red nuclei (RN). These lie just dorsal of the substantia nigra (SN), and slightly posterior to the subthalamic nucleus (STN). [Color figure can be viewed at wileyonlinelibrary.com]

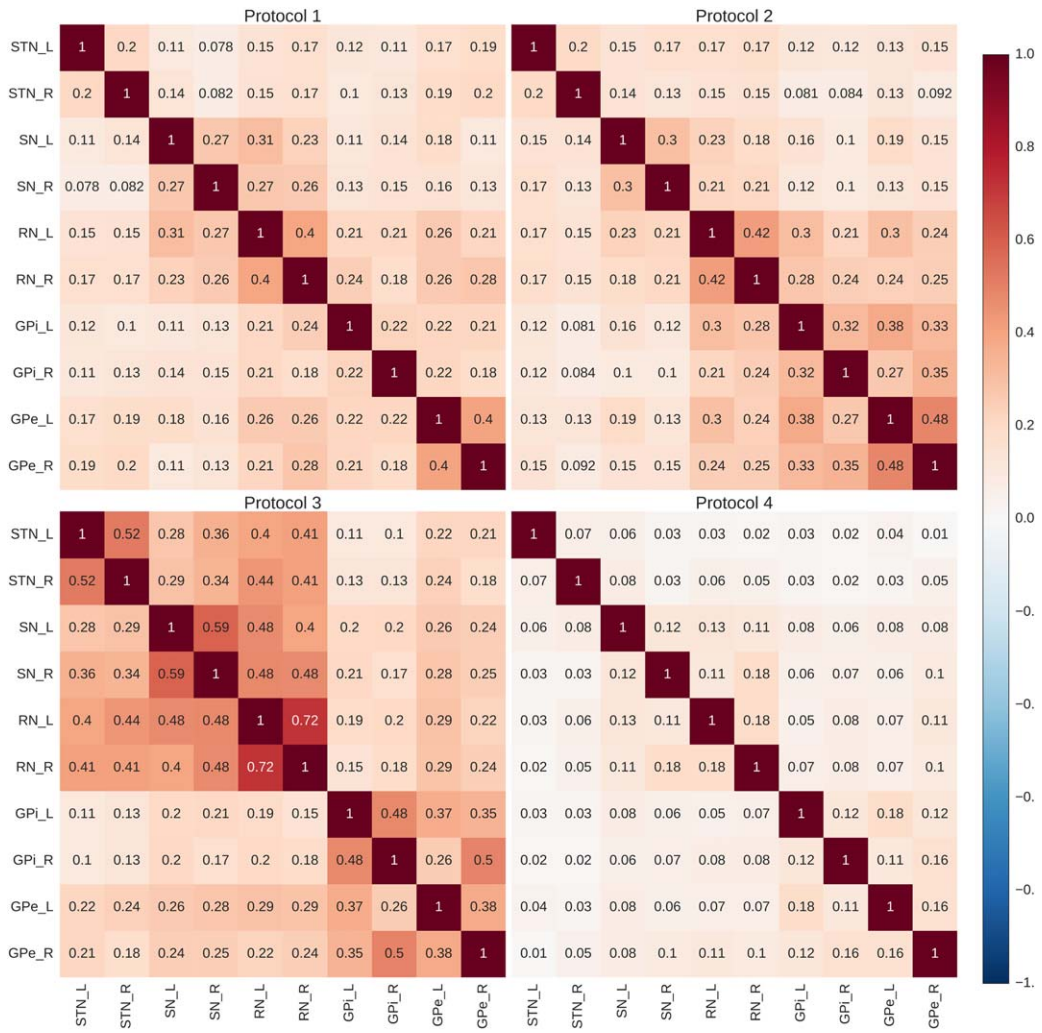

Figure 12.

Mean Basal Ganglia functional connectomes for the four protocols. Note how in protocol 1–3 (and especially in protocol 3) contralateral homologues are more strongly correlated than ipsilateral nodes that are spatially much closer. For example, the timeseries in left and right STN are more correlated than those of left STN and left SN, even though they lie adjacent to each other. This suggests some functional relevance of the found correlations, more than just spatially correlated (physiological) noise. [Color figure can be viewed at wileyonlinelibrary.com]

Importantly, the correlation sizes were in general higher in protocol 3 (1.5 mm/14 ms/7 T), especially in STN, SN, and RN (see Fig. 12). These higher correlations are to be expected because of the higher tSNR of this protocol compared with protocols 1 (1.2 mm/22 ms/7 T), 2 (1.2 mm/15 ms/7 T), and 4 (1.5 mm/30 ms/3 T).

DISCUSSION

The BG plays a crucial role in many cognitive paradigms and they are thought to subserve diverse cognitive functions such as decision-making and learning. However, it remains a challenge to functionally image the BG with sufficient anatomical detail to attribute measured signals to specific nodes and their putative subdivisions [De Hollander et al., 2015]. Here we tested three fMRI protocols at 7 T, as well as a comparable protocol at 3 T, to quantitatively test which set of scanning parameters (most notably echo time, resolution, and field strength), deliver robust BOLD sensitivity with maximal anatomical specificity.

First and foremost, our work establishes that, compared with functional neuroimaging of the cortex, some modesty in terms of resolution is necessary and special care should be taken to accommodate the short effective T2* relaxation values in and close to the iron-rich BG nuclei, especially at

higher field strengths. Using a spatial resolution of 1.2 mm isotropic and a GRAPPA factor of 4, parameters that are frequently used in "cortical" 7 T functional neuroimaging studies [Van der Zwaag et al., 2016], we found no robust BOLD sensitivity in subcortical BG nuclei. Even when the echo time was specifically optimized for these nuclei (protocol 2), voxelwise tSNRs were very low. The average task-locked signal did not resemble a hemodynamic response and statistical tests showed no task-related activity or significant differences between task conditions. A different picture emerged for the 1.5 mm isotropic 7 T fMRI protocol with a GRAPPA factor of 3 (protocol 3). This protocol showed significant task-related activity in all conditions, with the same limited number of subjects (5). This protocol is similar to earlier work that showed activations in the BG nuclei [Keuken et al., 2015; Mestres-Missé et al., 2017].

We also tried to replicate a high-resolution 3 T fMRI protocol with 1.5 mm isotropic resolution focusing on BG nodes [Pauli et al., 2015]. This protocol showed no robust BOLD sensitivity. More specifically, voxelwise tSNR was very low, the average task-locked signal did not resemble a hemodynamic response, and, after FDR correction, no BG nuclei showed significant activation. One may argue that the differences between the findings by Pauli et al. and our findings can be attributed to differences in the analysis, preprocessing, and experimental paradigm as follows: (a) we performed a relatively stringent a-priori anatomical-region-of-interest analysis. This was different from the voxelwise analysis without (explicit) multiple comparison correction in Pauli et al. In their study, the data were thresholded at arbitrary and relatively lenient (especially considering the high resolution and limited smoothing) one-sided thresholds of $P < 0.005$ and $P < 0.001$; (b) here, no physiological filtering of the fMRI data was performed (since no physiological data were available for this protocol); (c) we used a different experimental paradigm that taps into action selection and response inhibition, rather than (passive) reinforcement learning.

Despite our current findings, it is important to note that functional neuroimaging at a lower field strength of 3 T still has some advantages over UHF MRI in terms of lower costs, reduced geometrical distortions, less T_2* variability, and higher T_2* values across the brain (attenuating the need for very short echo times). However, it is also evident from the current results that the 7 T MRI protocol used in the present study provides superior tSNR at an appropriate spatial resolution to achieve sufficient anatomical specificity in BG nodes. We suggest that special care should be taken in future studies investigating the subcortex, in particular BG nodes, with 3 T fMRI.

Secondly, this study suggests that the BG nuclei are highly similar in their activation patterns during the different conditions of the stop-signal task. Specifically, all nodes show increased activity compared with baseline in both go and failed stops, as well as during successful stopping trials. Moreover, most of the BG nuclei showed increased activity during failed stop compared with go and successful stop trials. Contrary to the findings of Aron et al. [2006] in an "STN region" that probably corresponds to a combination of the subcortex BG nuclei studied here, no BG nuclei showed heightened activity in successful stop trials compared with go trials [but see Aron et al., 2014a, 2015; Cai et al., 2014; Erika-Florence et al., 2014; Hampshire, 2015; Hampshire and Sharp, 2015]. A difference in activation between failed stop and go trials, but no difference between successful stop and go trials in the "STN region" has been reported before in other studies [Jahfari et al., 2011; Ray Li et al., 2008]. Multiple theoretical frameworks have been developed that might help further interpret these findings in future work [Hampshire and Sharp, 2015; Shenoy and Yu, 2011].

Thirdly, the present study shows that the traditional analysis approach where individual SPMs are transformed to a MNI152 standard space using T_1-weighted anatomical images after smoothing with a moderate 5mm FWHM Gaussian kernel, leads to a severe loss of anatomical detail. The activation clusters that were found in the "failed stop > go" contrast cover almost the entire subcortex and brainstem. A more specific approach that uses a-priori defined individual anatomical masks and/or a group-specific T_2* weighted template provided more fine grained anatomical specificity. Such specificity is necessary for the validation of current detailed models of BG functioning. Theoretical, simulation, and meta-analysis articles have all stressed the negative influence of smoothing on anatomical specificity [de Hollander et al., 2015; Stelzer, 2014; Turner and Geyer, 2014].

Lastly, the explorative voxelwise analysis in the group template shows that subcortical areas other than the main BG nuclei are also involved in the stop signal task, mostly in the thalamus and brainstem, and possibly in the VTA. Unfortunately, the field of neuroimaging is currently lacking detailed subcortical atlases that allow us to probe these areas in more detail and this work motivates further work on the extension of subcortical MRI atlases [there are potentially hundreds of distinct subcortical areas; Alkemade et al., 2013; Keuken et al., 2014].

FUTURE WORK

The current results shed new light on the pressing issue to develop new UHF fMRI protocols specifically tailored to subcortical brain structures [Van der Zwaag et al., 2016]. The greatest challenge will be to increase the SNR, allowing for higher resolutions and sensitivity to detect small differences in activity due to experimental manipulations in cognitive paradigms. There are several directions of future work that could help to increase the SNR in the subcortex: (1) rapid acquisition techniques, such as simultaneous multi slice (SMS) and accelerated 3D image encoding. These techniques do not subsequently acquire single

2D slices, but multiple slices or entire brain volumes simultaneously [Boyacioğlu et al., 2015; Setsompop et al., 2016]. This allows for reducing TR and the collection of more volumes and/or slices per experiment; (2) the use of multi-echo protocols that yield multiple images with different echo times, collected virtually at the same time. These different images could be used to have an optimal signal across the entire brain, including areas with vastly different T_2* baseline values [Koopmans et al., 2011; Kundu et al., 2012]; (3) coil setups tailored toward deep brain structures. Currently, multi-channel coil arrays have a high number of coils that are locally sensitive, which facilitates parallel imaging techniques, but effectively only in the "outer" parts of the brain [De Zwart et al., 2002; Pruessmann et al., 1999; Setsompop et al., 2016]. This local sensitivity can be detrimental to the sensitivity in the deeper parts of the brain, since they are relatively distant from all the coils in the array.

Furthermore, the effective resolution of fMRI can also be further improved by using contrast mechanisms that are more tightly localized than the default BOLD contrast. One promising candidate would be the Vascular Space Occupancy sequence (VASO) that is sensitive to cerebral blood volume (CBV), affording higher spatial specificity to the activated nuclei, especially at higher field strengths [Huber et al., 2014, 2016; Lu et al., 2003]. Unfortunately, the increased specificity comes at a cost of reduced signal sensitivity, and future work should test whether VASO can be an effective functional measure not only in cortical, but also subcortical areas. Another possibility is the use of Spin Echo-based protocols (SE). There is a large amount of large vessels present in the subcortex. The T_2 contrast that SE protocols offer are less sensitive to draining veins and thus would be more spatially specific to activation of the nuclei themselves [Parkes et al., 2005; Uludağ et al., 2009]. Furthermore, Spin Echo-based sequences are less sensitive to susceptibility effects induced by iron deposition. However, those advantages come with a decreased overall BOLD sensitivity and an increased specific absorption rate, especially at UHF, limiting the spatial coverage of the acquisition.

Parallel efforts could focus on improving the sensitivity of functional MRI at the lower field strength of 3 T. Although the SNR is inherently lower at 3 T compared with 7 T, 3 T scanners are much more widely available and have lower operating costs. Future work should thoroughly establish whether robust BOLD sensitivity can or cannot be achieved at 3 T without severely sacrificing anatomical specificity. One possible approach would be to slightly reduce the resolution of the functional images but still use high-quality anatomical data for precise localization of the nuclei-of-interest. The problem of lower SNR might also be somewhat overcome by longer acquisitions and massive averaging, but note that one needs roughly $(7/3)^2 = 5.4$ times more data to obtain similar signal estimation at 3 T versus 7 T, ignoring issues like subject movement and fatigue (the subjects already performed the task for 51 minutes in the protocols described in this article). Although some 3 T studies have convincingly shown activation clusters in subcortical BG nodes, the issue of anatomical specificity of activation clusters has oftentimes been overlooked [de Hollander et al., 2015].

CONCLUSION

In sum, the Basal Ganglia play a crucial role in theories of cognition and disease and the study of their functioning could help elucidate the neural underpinnings of therapies such as DBS and cognitive processes such as response inhibition. Functional imaging of these nuclei with sufficient anatomical detail in the living human is, however, a challenging endeavor. Special caution should be taken in the development of UHF fMRI protocols targeting the BG, because the magnetic properties of these small iron-rich nuclei are considerably different from cortical regions, the usual focus of UHF fMRI studies. The study described here provides a first recipe for a validated fMRI protocol at 7 T that can disentangle signals originating from different subparts of this subcortical network.

ACKNOWLEDGMENTS

We would like to thank Domenica Wilfing and Elisabeth Wladimirow for their help in acquiring the data.

REFERENCES

Alexander GE, Crutcher MD (1990): Functional architecture of basal ganglia circuits: neural substrates of parallel processing. Trends Neurosci 13:266–271.

Alkemade A, Keuken MC, Forstmann BU (2013): A perspective on terra incognita: uncovering the neuroanatomy of the human subcortex. Front Neuroanat 7:40.

Aquino D, Bizzi A, Grisoli M, Garavaglia B, Bruzzone MG, Nardocci N, Savoiardo M, Chiapparini L (2009): Age-related iron deposition in the basal ganglia: quantitative analysis in healthy subjects. Radiology 252:165–172.

Aron AR (2007): The neural basis of inhibition in cognitive control. Neuroscientist 13:214–228.

Aron AR, Poldrack RA (2006): Cortical and subcortical contributions to Stop signal response inhibition: role of the subthalamic nucleus. Journal of Neuroscience 26:2424–2433.

Aron AR (2011): From reactive to proactive and selective control: developing a richer model for stopping inappropriate responses. Biol Psychiatry 69:e55–e68.

Aron AR, Robbins TW, Poldrack RA (2014a): Right inferior frontal cortex: addressing the rebuttals. Front Hum Neurosci 8:905.

Aron AR, Robbins TW, Poldrack RA (2014b): Inhibition and the right inferior frontal cortex: one decade on. Trends Cogn Sci 18:177–185.

Aron AR, Cai W, Badre D, Robbins TW (2015): Evidence supports specific braking function for inferior PFC. Trends Cogn Sci 1–2.

Arsenault JT, Rima S, Stemmann H, Vanduffel W (2014): Role of the primateventral tegmental areain reinforcement and motivation. Curr Biol 85:1155–1157.

Avants BB, Tustison N, Song G (2009): Advanced normalization tools (ANTS). Insight J 2:1–35.

Barry RL, Strother SC, Gatenby JC, Gore JC (2011): Data-driven optimization and evaluation of 2D EPI and 3D PRESTO for BOLD fMRI at 7 Tesla: I. Focal coverage. Neuroimage 1–10.

Barry RL, Coaster M, Rogers BP, Newton AT, Moore J, Anderson AW, Zald DH, Gore JC (2013): On the origins of signal variance in fmri of the human midbrain at high field. PLoS ONE 8:e62708.

Bazin P-L, Cuzzocreo JL, Yassa MA, Gandler W, McAuliffe MJ, Bassett SS, Pham DL (2007): Volumetric neuroimage analysis extensions for the MIPAV software package. J Neurosci Methods 165:111–121.

Bogacz R, Gurney K (2007): The basal ganglia and cortex implement optimal decision making between alternative actions. Neural Comput 19:442–477.

Boyacioğlu R, Schulz J, Koopmans PJ, Barth M, Norris DG (2015): Improved sensitivity and specificity for resting state and task fMRI with multiband multi-echo EPI compared to multi-echo EPI at 7T. Neuroimage 119:352–361.

Brett M, Taylor J, Burns C, Millman KJ, Perez F, Roche A, Thirion B, D'Esposito M (2009): NIPY: an open library and development framework for FMRI data analysis. Neuroimage 47:S196.

Cai W, Ryali S, Chen T, Li CSR, Menon V (2014): Dissociable roles of right inferior frontal cortex and anterior insula in inhibitory control: evidence from intrinsic and task-related functional parcellation, connectivity, and response profile analyses across multiple datasets. J Neurosci 34:14652–14667.

de Hollander G, Keuken MC, Bazin P-L, Weiss M, Neumann J, Reimann K, Wähnert M, Turner R, Forstmann BU, Schäfer A (2014): A gradual increase of iron toward the medial-inferior tip of the subthalamic nucleus. Hum Brain Mapp 35:4440–4449.

de Hollander G, Keuken MC, Forstmann BU (2015): the subcortical cocktail problem; mixed signals from the subthalamic nucleus and substantia nigra. Ed. Bogdan Draganski. PLoS ONE 10:e0120572.

de Zwart JA, van Gelderen P, Kellman P, Duyn JH (2002): Application of sensitivity-encoded echo-planar imaging for blood oxygen level-dependent functional brain imaging. Magn Reson Med 48:1011–1020.

Deistung A, Schäfer A, Schweser F, Biedermann U, Turner R, Reichenbach JR (2013): Toward in vivo histology: A comparison of quantitative susceptibility mapping (QSM) with magnitude-, phase-, and R2*-imaging at ultra-high magnetic field strength. Neuroimage 65:299–314.

Dice LR (1945): Measures of the amount of ecologic association between species. Ecology 26:297–302.

Eapen M, Zald DH, Gatenby JC, Ding Z, Gore JC (2011): Using high-resolution MR imaging at 7T to evaluate the anatomy of the midbrain dopaminergic system. Am J Neuroradiol 32: 688–694.

Erika-Florence M, Leech R, Hampshire A (2014): A functional network perspective on response inhibition and attentional control. Nat Commun 5:1–12.

Fasano A, Lozano AM (2015): Deep brain stimulation for movement disorders. Curr Opin Neurol 28:423–436.

Forstmann BU, Keuken MC, Schäfer A, Bazin P-L, Alkemade A, Turner R (2014): Multi-modal ultra-high resolution structural 7-Tesla MRI data repository. Sci Data 1:140050.

Frank MJ (2006): Hold your horses: A dynamic computational role for the subthalamic nucleus in decision making. Neural Netw 19:1120–1136.

Frank MJ, Claus ED (2006): Anatomy of a decision: Striato-orbitofrontal interactions in reinforcement learning, decision making, and reversal. Psychol Rev 113:300–326.

Glover GH (1999): Deconvolution of impulse response in event-related BOLD fMRI. Neuroimage 9:416–429.

Glover GH, Li TQ, Ress D (2000): Image-based method for retrospective correction of physiological motion effects in fMRI: RETROICOR. Magn Reson Med 44:162–167.

Gorgolewski K, Burns CD, Madison C (2011): Nipype: a flexible, lightweight and extensible neuroimaging data processing framework in python. Front Neuroinform 3:8.

Griswold MA, Jakob PM, Heidemann RM, Nittka M, Jellus V, Wang J, Kiefer B, Haase A (2002): Generalized autocalibrating partially parallel acquisitions (GRAPPA). Magn Reson Med 47: 1202–1210.

Gurney K, Prescott TJ, Redgrave P (2001): A computational model of action selection in the basal ganglia. I. A new functional anatomy. Biol Cybern 84:401–410.

Haase A, Frahm J, Matthaei D, Hanicke W, Merboldt KD (1985): FLASH imaging. Rapid NMR imaging using low flip-angle pulses. J Magn Reson (1969-1992) 67:258–266.

Haber SN (2014): The place of dopamine in the cortico-basal ganglia circuit. Neuroscience 282:248–257.

Hampshire A (2015): Putting the brakes on inhibitory models of frontal lobe function. Neuroimage 113:340–355.

Hampshire A, Sharp DJ (2015): Contrasting network and modular perspectives on inhibitory control. Trends Cogn Sci 19:445–452.

Huber L, Ivanov D, Krieger SN, Streicher MN, Mildner T, Poser BA, Möller HE, Turner R (2014): Slab-selective, BOLD-corrected VASO at 7 Tesla provides measures of cerebral blood volume reactivity with high signal-to-noise ratio. Magn Reson Med 72:137–148.

Huber L, Ivanov D, Guidi M, Turner R, Uludağ K, Möller HE, & Poser BA (2016): Functional cerebral blood volume mapping with simultaneous multi-slice acquisition. Neuroimage 125: 1159–1168.

Ineichen C, Glannon W, Temel Y, Baumann CR, Sürücü O (2014): A critical reflection on the technological development of deep brain stimulation (DBS). Front Hum Neurosci 8:730.

Jahfari S, Waldorp L, van den Wildenberg WPM, Scholte HS, Ridderinkhof KR, Forstmann BU (2011): Effective connectivity reveals important roles for both the hyperdirect (fronto-subthalamic) and the indirect (fronto-striatal-pallidal) fronto-basal ganglia pathways during response inhibition. J Neurosci 31:6891–6899.

Jenkinson M, Smith S (2001): A global optimisation method for robust affine registration of brain images. Med Image Anal 5: 143–156.

Keren NI, Taheri S, Vazey EM, Morgan PS, Granholm A-CE, Aston-Jones GS, Eckert MA (2015): Histologic validation of locus coeruleus MRI contrast in post-mortem tissue. Neuroimage 113:235–245.

Keuken MC, Uylings HBM, Geyer S, Schäfer A, Turner R, Forstmann BU (2012): Are there three subdivisions in the primate subthalamic nucleus?. Front Neuroanat 6:14.

Keuken MC, Bazin PL, Schäfer A, Neumann J, Turner R, Forstmann BU (2013): Ultra-high 7T MRI of structural age-related changes of the subthalamic nucleus. J Neurosci 33:4896–4900.

Keuken MC, Bazin PL, Crown L, Hootsmans J, Laufer A, Müller-Axt C, Sier R, van der Putten EJ, Schäfer A, Turner R, Forstmann

BU (2014): Quantifying inter-individual anatomical variability in the subcortex using 7T structural MRI. Neuroimage 94:40–46.

Keuken MC, van Maanen L, Bogacz R, Schäfer A, Neumann J, Turner R, Forstmann BU (2015): The subthalamic nucleus during decision-making with multiple alternatives. Hum Brain Mapp 36:4041–4052.

Keuken MC, Bazin PL, Backhouse K, Beekhuizen S, Himmer L, Kandola A, Lafeber JJ, Prochazkova L, Trutti A, Schäfer A, Turner R, Forstmann BU (2017): Effects of aging on T1, T2*, and QSM MRI values in the subcortex. Brain Struct Funct. http://doi.org/10.1007/s00429-016-1352-4

Koopmans PJ, Barth M, Orzada S, Norris DG (2011): Multi-echo fMRI of the cortical laminae in humans at 7T. Neuroimage 56: 1276–1285.

Kundu P, Inati SJ, Evans JW, Luh W-M, Bandettini PA (2012): Differentiating BOLD and non-BOLD signals in fMRI time series using multi-echo EPI. Neuroimage 60:1759–1770.

Langkammer C, Schweser F, Krebs N, Deistung A, Goessler W, Scheurer E, Sommer K, Reishofer G, Yen K, Fazekas F, Ropele S, Reichenbach JR (2012): Quantitative susceptibility mapping (QSM) as a means to measure brain iron? A post mortem validation study. Neuroimage 62:1593–1599.

Linnman C, Moulton EA, Barmettler G, Becerra L, Borsook D (2012): Neuroimaging of the periaqueductal gray: State of the field. Neuroimage 60:505–522.

Logan GD, Cowan WB (1984): On the ability to inhibit thought and action: A theory of an act of control. Psychol Rev 91:295.

Logan GD, Cowan WB, Davis KA (1984): On the ability to inhibit simple and choice reaction time responses: a model and a method. J Exp Psychol 10:276–291.

Logothetis NK (2008): What we can do and what we cannot do with fMRI. Nature 453:869–878.

Lu H, Golay X, Pekar JJ, van Zijl PCM (2003): Functional magnetic resonance imaging based on changes in vascular space occupancy. Magn Reson Med 50:263–274.

Lutti A, Dick F, Sereno MI, & Weiskopf N (2014): Using high-resolution quantitative mapping of R1 as an index of cortical myelination. Neuroimage, 93:176–188.

Marques JP, Kober T, Krueger G, Van der Zwaag W, van de Moortele P-F, Gruetter R (2010): MP2RAGE, a self bias-field corrected sequence for improved segmentation and T1-mapping at high field. Neuroimage 49:1271–1281.

McAuliffe MJ, Lalonde FM, McGarry D, Gandler W, Csaky K, Trus BL (2001): Medical Image Processing, Analysis and Visualization in clinical research. pp 381–386. http://ieeexplore.ieee.org/xpls/abs_all.jsp?arnumber=941749.

Mestres-Missé A, Trampel R, Turner R, & Kotz SA (2017): Uncertainty and expectancy deviations require cortico-subcortical cooperation. Neuroimage 144(Pt A):23–34.

Middleton FA, Strick PL. (2000) A revised neuroanatomy of the fronto-subcortical circuits. In: Lichter DG, Cummings JL, eds. Frontal-subcortical Circuits in Psychiatric and Neurological Disorders. New York, NY: The Guilford Press. pp 44–58.

Morey RD, Rouder JN (2015): *BayesFactor: An R package for computing Bayes factors in common research designs*. bayesfactorpcl.r-forge.r-project.org. http://bayesfactorpcl.r-forge.r-project.org/.

Murphy K, Bodurka J, Bandettini PA (2007): How long to scan? The relationship between fMRI temporal signal to noise ratio and necessary scan duration. Neuroimage 34:565–574.

Neath AA, & Cavanaugh JE (2006): A Bayesian approach to the multiple comparisons problem. J Data Sci, 4:131–146.

Norris DG (2006): Principles of magnetic resonance assessment of brain function. J Magn Reson Imaging 23:794–807.

Ogawa S, Lee TM, Kay AR, Tank DW (1990): Brain magnetic resonance imaging with contrast dependent on blood oxygenation. Proc Natl Acad Sci 87:9868–9872.

Oldfield RC (1971): The assessment and analysis of handedness: the Edinburgh inventory. Neuropsychologia 9:97–113.

Parent A, Hazrati L-N (1995): Functional anatomy of the basal ganglia. I. The cortico-basal ganglia-thalamo-cortical loop. Brain Res Rev 20:91–127.

Parkes LM, Schwarzbach JV, Bouts AA, Deckers RHR, Pullens P, Kerskens CM, Norris DG (2005): Quantifying the spatial resolution of the gradient echo and spin echo BOLD response at 3 Tesla. Magn Reson Med 54:1465–1472.

Pauli WM, Larsen T, Collette S, Tyszka JM, Seymour B, O'Doherty JP (2015): Distinct contributions of ventromedial and dorsolateral subregions of the human substantia nigra to appetitive and aversive learning. J Neurosci 35:14220–14233.

Peters AM, Brookes MJ, Hoogenraad FG, Gowland PA, Francis ST, Morris PG, Bowtell R (2007): T2* measurements in human brain at 1.5, 3 and 7 T. Magn Reson Imaging 25:748–753.

Plantinga BR, Temel Y, Roebroeck A, Uludağ K, Ivanov D, Kuijf ML, Haar Romenij ter BM (2014): Ultra-high field magnetic resonance imaging of the basal ganglia and related structures. Front Hum Neurosci 8:876.

Poldrack RA, Mumford JA, Nichols TE (2011): Statistical modelling: Single subject analysis. In: Poldrack RA, Mumford JA, Nichols TE, editors. Handbook of Functional MRI Analysis, 1st ed. Cambridge: Cambridge University Press. pp 70–99.

Pruessmann KP, Weiger M, Scheidegger MB, Boesiger P (1999): SENSE: sensitivity encoding for fast MRI. Magn Reson Med 42:952–962.

Ray Li C-S, Yan P, Sinha R, Lee T-W (2008): Subcortical processes of motor response inhibition during a stop signal task. Neuroimage 41:1352–1363.

Redgrave P, Prescott TJ, Gurney K (1999): The basal ganglia: a vertebrate solution to the selection problem?. Neuroscience 89: 1009–1023.

Redgrave P, Rodriguez M, Smith Y, Rodriguez-Oroz MC, Lehericy S, Bergman H, Agid Y, DeLong MR, Obeso JA (2010): Goal-directed and habitual control in the basal ganglia: implications for Parkinson's disease. Nat Rev Neurosci 11:1–13.

Rouder JN, Morey RD, Speckman PL, Province JM (2012): Default Bayes factors for ANOVA designs. J Math Psychol 56:356–374.

Schäfer A, Forstmann BU, Neumann J, Wharton S, Mietke A, Bowtell R, Turner R (2011): Direct visualization of the subthalamic nucleus and its iron distribution using high-resolution susceptibility mapping. Hum Brain Mapp 33:2831–2842.

Schweser F, Deistung A, Lehr BW, Reichenbach JR (2011): Quantitative imaging of intrinsic magnetic tissue properties using MRI signal phase: An approach to in vivo brain iron metabolism?. Neuroimage 54:2789–2807.

Seabold S, Perktold J (2010): Statsmodels: Econometric and statistical modeling with python. In: Proceedings of the 9th Pythonin Science Conference. pp 57–61.

Setsompop, K., Feinberg, D. A., & Polimeni, J. R. (2016): Rapid brain MRI acquisition techniques at ultra-high fields. NMR Biomed 29: 1198–1221.

Shenoy P, Yu AJ (2011): Rational decision-making in inhibitory control. Front Hum Neurosci 5:48.

Smith SM (2002): Fast robust automated brain extraction. Hum Brain Mapp 17:143–155.

Smith SM, Jenkinson M, Woolrich MW, Beckmann CF, Behrens TEJ, Johansen-Berg H, Bannister PR, De Luca M, Drobnjak I, Flitney DE, others. (2004): Advances in functional and structural MR image analysis and implementation as FSL. Neuroimage 23:S208–S219.

Sodickson DK, Manning WJ (1997): Simultaneous acquisition of spatial harmonics (SMASH): fast imaging with radiofrequency coil arrays. Magn Reson Med 38:591–603.

Stelzer J, Lohmann G, Mueller K, Buschmann T, Turner R. (2014): Deficient approaches to human neuroimaging. Frontiers in Human Neuroscience 8:462.

Stephens M, Balding DJ (2009): Bayesian statistical methods for genetic association studies. Nat Rev Genet 10:681–690.

Temel Y, Blokland A, Steinbusch HWM, Visser-Vandewalle V (2005): The functional role of the subthalamic nucleus in cognitive and limbic circuits. Prog Neurobiol 76:393–413.

Triantafyllou C, Hoge RD, Krueger G, Wiggins CJ, Potthast A, Wiggins GC, Wald LL (2005): Comparison of physiological noise at 1.5 T, 3 T and 7 T and optimization of fMRI acquisition parameters. Neuroimage 26:243–250.

Triantafyllou C, Hoge RD, Wald LL (2006): Effect of spatial smoothing on physiological noise in high-resolution fMRI. Neuroimage 32:551–557.

Turner R, Geyer S (2014): Comparing like with like: the power of knowing where you are. Brain Connect 4:547–557.

Uludağ K, Müller-Bierl B, Uğurbil K (2009): An integrative model for neuronal activity-induced signal changes for gradient and spin echo functional imaging. Neuroimage 48:150–165.

Van der Zwaag W, Francis S, Head K, Peters A, Gowland P, Morris P, Bowtell R (2009): fMRI at 1.5, 3 and 7 T: Characterising BOLD signal changes. Neuroimage 47:1425–1434.

Van der Zwaag W, Jorge J, Butticaz D, Gruetter R (2015): Physiological noise in human cerebellar fMRI. Magn Reson Mater Phys 28:485–492.

Van der Zwaag W, Schäfer A, Marques JP, Turner R, Trampel R (2016): Recent applications of UHF-MRI in the study of human brain function and structure: a review. NMR Biomed 29:1274–1288.

Verbruggen F, Logan GD (2009): Models of response inhibition in the stop-signal and stop-change paradigms. Neurosci Biobehav Rev 33:647–661.

Wagenmakers E-J (2007): A practical solution to the pervasive problems of p values. Psychon Bull Rev 14:779–804.

Weiskopf N, Callaghan MF, Josephs O, Lutti A, Mohammadi S (2014): Estimating the apparent transverse relaxation time (R2(*)) from images with different contrasts (ESTATICS) reduces motion artifacts. Front Neurosci 8:278.

Woolrich MW, Jbabdi S, Patenaude B, Chappell M, Makni S, Behrens T, Beckmann C, Jenkinson M, Smith SM (2009): Bayesian analysis of neuroimaging data in FSL. Neuroimage 45: S173–S186.

Worsley KJ, Friston KJ (1995): Analysis of fMRI time-series revisited—again. Neuroimage 2:173–181.

Yacoub E, Shmuel A, Pfeuffer J, Van De Moortele PF, Adriany G, Andersen P, Vaughan JT, Merkle H, Ugurbil K, HU X (2001): Imaging brain function in humans at 7 Tesla. Magn Reson Med 45:588–594.

Zwirner J, Möbius D, Bechmann I, Arendt T, Hoffmann K-T, Jäger C, Lobsien D, Möbius R, Planitzer U, Winkler D, Morawski M, Hammer N (2017): Subthalamic nucleus volumes are highly consistent but decrease age-dependently-a combined magnetic resonance imaging and stereology approach in humans. Hum Brain Mapp 38:909–922.